

In this case either the state vector \mathbf{x} may be too limited or the operators contain errors. An example is the omission of processes controlling the carbon cycle in GCMs used in IPCC-AR4, such as those in the marine and terrestrial biosphere.

Suppose we have decided on our model type, with appropriate parameterizations, fixed parameters and chosen forcing functions. Even when realising that such a model contains severe idealisations and has all types [(i)–(iv)] of errors, there are still important a priori checks that can be done before using such a model.

- (1) *Consistency.* When the continuous formulation is chosen (with all its idealisations and errors) and the discretisation method is chosen, it is very important to check that the grid and time step used provide sufficiently accurate results to these equations. Hence for fixed parameters, it is always necessary to perform calculations with different grid sizes and time steps to investigate whether one solves the ‘correct’ equations (the equations one intends to solve).
- (2) *Integral balances.* For every model, one can integrate the continuous equations used over the domain and obtain usually much more simplified integral equations, representing overall conservation of mass/energy and heat/salt components. For a solution of the discrete model, the discrete integral balances should be satisfied up to a certain accuracy, say a relative error (with respect to the largest term) of a few percentages. Numerical solutions where mass, energy and so forth have large artificial sources or sinks in the system are meaningless.

With this overview of the hierarchy of models and their error sources, we are now ready to tackle several important problems in climate physics using dynamical systems theory as will be done in the next chapters.

7

The North Atlantic Oscillation

Timing is strange, but the pattern is clear.

CGEGBD, The Unexpected Visitor. Michael Hedges

As a first application of stochastic dynamical systems theory to understand phenomena of climate variability, we consider midlatitude atmospheric variability with a focus on the North Atlantic.

7.1 Midlatitude atmospheric variability

The midlatitude atmosphere varies on many time scales and spatial scales, and from daily weather maps we see the high and low pressure systems moving seemingly irregularly from west to east. When longer time scales than the synoptic weather time scale (1–10 days) are considered, it appears that some patterns of variability appear more frequently than others. Variability on time scales larger than 10 days is referred to as low-frequency variability (LFV). The patterns of this LFV exert an organizing

tendency on the weather and hence may be important for weather predictability on time scales longer than 10 days.

7.1.1 Low-frequency variability

The total root mean square (rms) Northern Hemispheric (NH) 500 hPa geopotential height variance (in m) during the winter season over the years 1958–1999 is plotted in Fig. 7.1a. The LFV component of this variability obtained by a low-pass (>10 days) filter (Fig. 7.1b) represents a substantial component that is about a factor 3 larger (Fig. 7.1c) than the variability on the synoptic scale (2.5–6 days). The maxima in the LFV component (Fig. 7.1b) are almost equal in amplitude to those in total variance (Fig. 7.1a) and almost precisely collocated with them. Two of these winter maxima occur over the northeastern part of the North Pacific and North Atlantic, the third over the Siberian Arctic. The maxima in the ‘weather band’ (Fig. 7.1c) occur slightly upstream of the LFV maxima, mainly over the storm tracks off the east coasts of North America and Asia.

There are a large number of studies on the patterns of LFV using many different methods and data sets. These patterns are determined to be related to two features: (i) intraseasonal oscillations and (ii) planetary flow (or weather) regimes (Ghil and Robertson, 2002). Intraseasonal oscillations are specific propagating patterns of variability with time scales in the range of 30–70 days. The planetary flow regimes are patterns that explain high variance and are classified according to hemispheric regimes (Section 7.1.3) or regional regimes (Section 7.1.4).

7.1.2 Intraseasonal oscillations

Signatures of intraseasonal variability were found (Dickey et al., 1991) in data of the global atmospheric angular momentum (AAM). Variations in global AAM and in the length of day are highly correlated with each other on intraseasonal time scales. Essentially, the Earth-atmosphere system is closed with respect to angular momentum exchanges on this time scale, except for the well-known tidal effects of the Sun and Moon, which can be easily computed and eliminated. When the strength of the midlatitude westerly winds increases or that of the tropical trade winds decreases, the solid earth slows down in its rotation, and the length of day increases. A power spectrum of the observed AAM variance for the NH extratropics (26°N – 90°N), see, for example, Fig. 7a in Dickey et al. (1991), indicates a peak at about 40 days, which is largely associated with fluctuations in the strength of the midlatitude westerlies.

Patterns of a 30- to 35-day oscillation in the NH winter have been found in 700 hPa geopotential height data using M-SSA (cf. Section 5.3.3) analysis. Phases of the oscillation are plotted in Fig. 7.2, where it can be seen that the dipole-type pressure anomalies with a dominant amplitude in the Atlantic region propagate westwards.

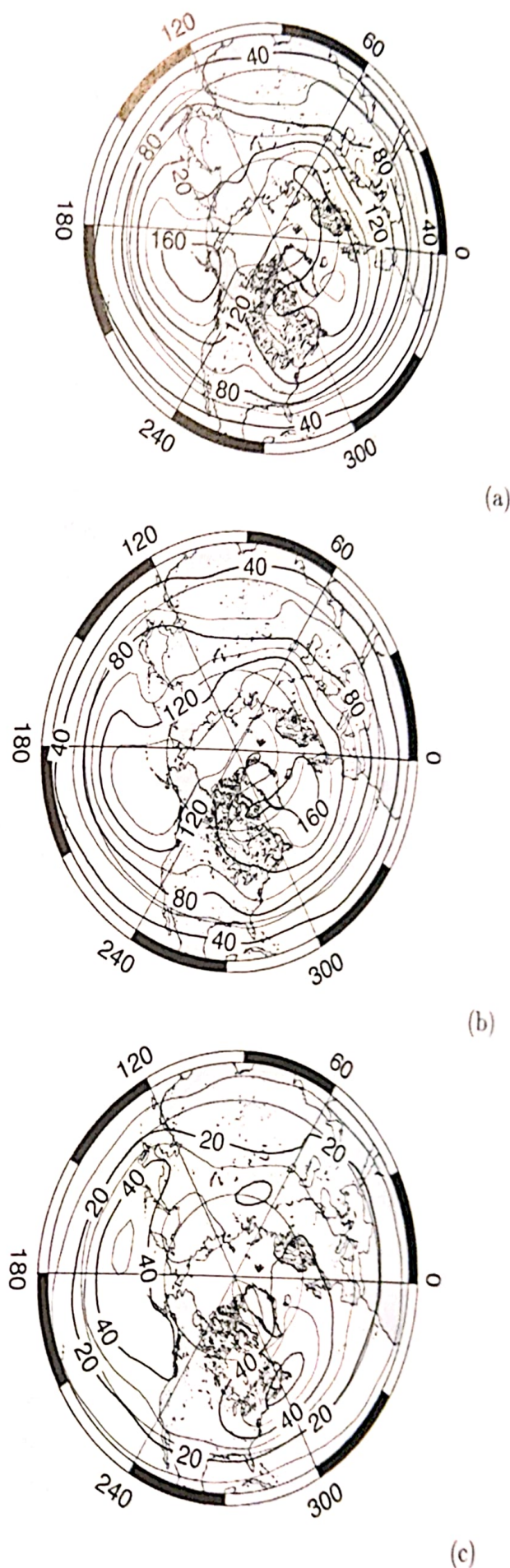


Figure 7.1 Maps of Northern Hemisphere 500-hPa geopotential height variance

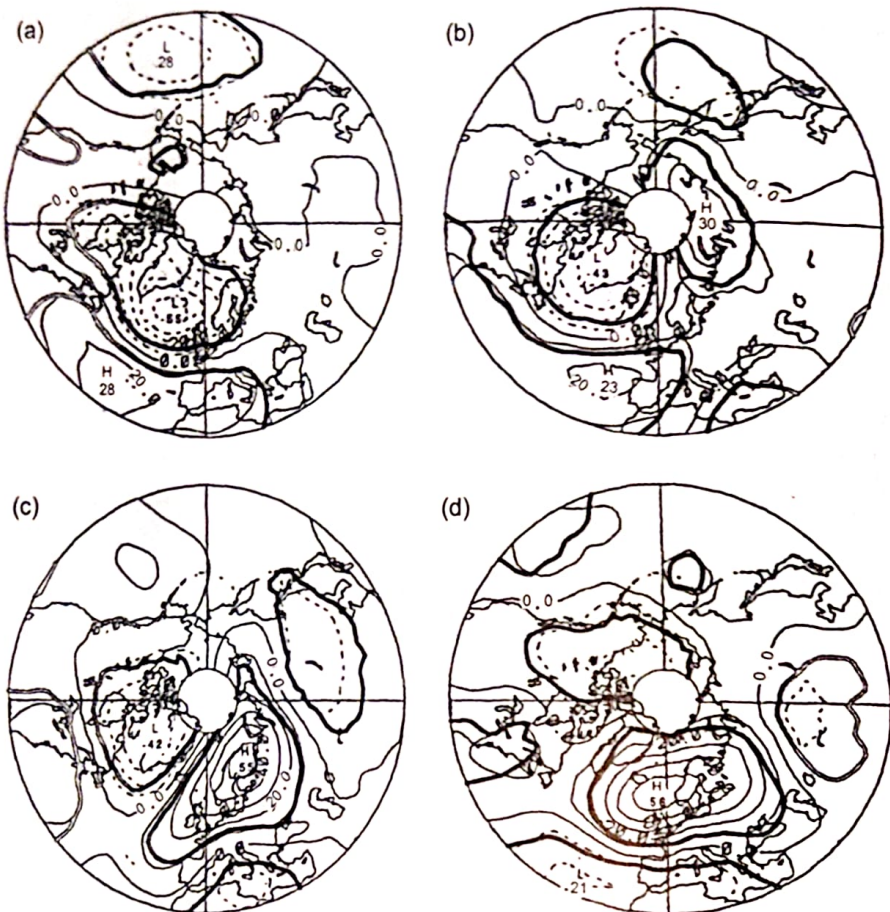


Figure 7.2 Different phases [time increases from (a) to (d)] of the pattern of 700 hPa geopotential height variability (dominant M-SSA mode, units in m) of the 30- to 35-day oscillation (figure from Plaut and Vautard [1994]).

In the same analysis (Plaut and Vautard, 1994), also intraseasonal oscillations with dominant periods of 40–45 days and 70 days are found. The 70-day oscillation consists of fluctuations in both position and amplitude of the Atlantic jet stream, with poleward-propagating anomaly patterns. The 40- to 45-day oscillation is specific to the Pacific sector.

7.1.3 Hemispheric weather regimes

The existence of hemispheric regimes is motivated by results (Wallace and Gutzler, 1981; Cheng and Wallace, 1993; Smyth et al., 1999) that suggest that circulation patterns with hemispheric coherence do exist or that regionally confined ones can be identified from hemispheric data. The hemispheric coherence may reflect a fundamental dynamical mode of the atmosphere, the Northern Annular Mode (NAM) (Thompson and Wallace, 2000; Thompson et al., 2000), also called the Arctic Oscillation, as shown in Fig. 7.3.

NAM

DJFM

23

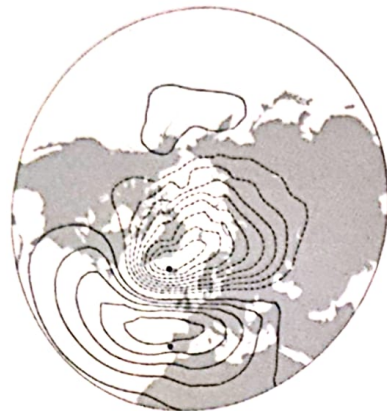


Figure 7.3 (a) Leading empirical orthogonal function (EOF 1) of the winter (December–March) mean sea level pressure (1899–2006) anomalies over the Northern Hemisphere (20°N – 90°N) and the percentage of the total variance it explains. The pattern is displayed in terms of amplitude (hPa, contour increment 0.5 hPa), obtained by regressing the hemispheric sea level pressure anomalies on the leading principal component time series, plotted in Fig. 7.4b (figure from Hurrell et al., 2003).

The NAM pattern is the leading EOF of nonseasonal sea level pressure variations north of 20°N latitude, and it is characterized by pressure anomalies of one sign in the Arctic with the opposite anomalies centered about 37°N – 45°N . The NAM is related to the degree to which Arctic air masses penetrate into midlatitudes. When the surface pressure anomaly is low in the polar region (positive NAM index), the midlatitude zonal winds are strong and cold Arctic air is locked in the polar region. When the NAM index is negative, there is relatively high pressure in the polar region with weaker zonal winds at midlatitudes and more movement of Arctic air southward. However, the NAM may also be a mere coincidence of separate regional patterns (Amabaum et al., 2001) that are discussed in the next section.

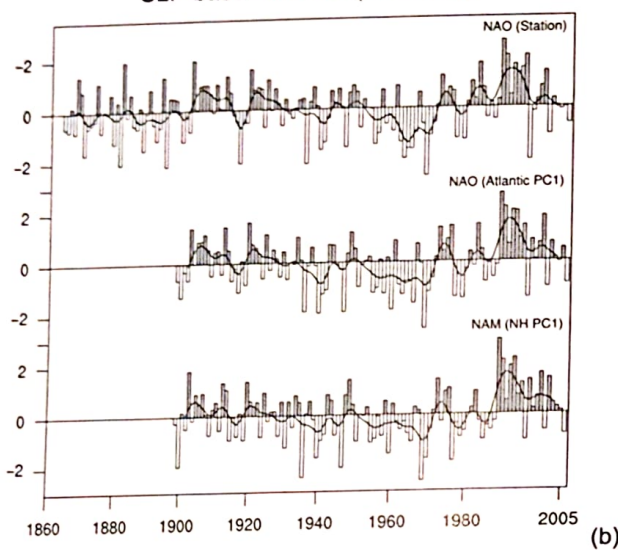
7.1.4 Regional weather regimes: Atlantic LFV

The regional classifications are motivated by evidence that the strongest patterns of Northern Hemispheric LFV are confined to either the Pacific/North American or the Atlantic-Eurasian sectors. When monthly mean anomalies of sea level pressure data over the North Atlantic region (20°N – 70°N ; 90°W – 40°E) are analysed for dominant patterns of variability, the first EOF (explaining 36% of the variance) for the DJFM season shows a pattern as in Fig. 7.4a. This is the pattern of the North Atlantic Oscillation (NAO), displayed here in terms of amplitude, obtained by regressing the hemispheric sea level pressure anomalies on the leading principal component (PC)

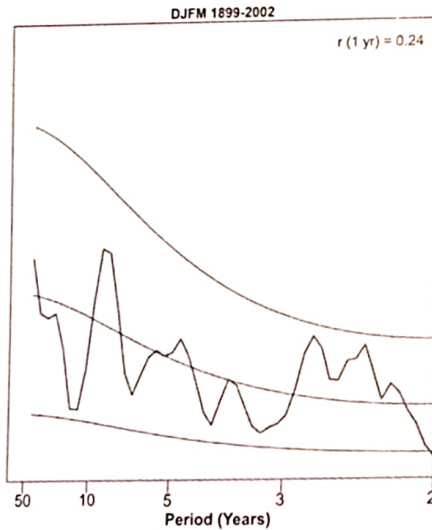


(a)

SLP-based Indices (Dec-Mar)



(b)



(c)

Figure 7.4 (a) Leading EOF of the DJFM mean sea level pressure anomalies (hPa contour increment 0.5 hPa) in the North Atlantic sector (20°N – 70°N ; 90°W – 40°E) over the years 1899–2001. (b) Normalised indices of the mean winter (December–March) NAO constructed from SLP data. Top panel: the difference of normalised sea level pressure between Lisbon and Stykkisholmur [dots in (a)]. Middle panel: the PC time series of the leading EOF as presented in (a). Lower panel: PC time series of the NAM. (c) Power spectrum of time series in the middle panel of (b) with the 5% and 95% confidence limits of the corresponding red noise spectrum; the lag-on autocorrelation coefficient is 0.24 (figure from Hurrell et al., 2003).

time series from the Atlantic domain, the NAO index. The centres with highest amplitude are located near Stykkisholmur (Iceland) and Lisbon (Portugal).

The winter-mean NAO index (Hurrell, 1995) based on station data (Lisbon-Stykkisholmur) is shown in the upper curve in Fig. 7.4b. The average winter sea level pressure data at each station were normalised by division of each seasonal pressure by the long-term mean (1864–1983) standard deviation. The station-based index for the winter season agrees well with PC1 of Atlantic-sector sea level pressure anomalies (middle curve). The correlation coefficient between the two is 0.92 over the common period 1899–2002, indicating that the station-based index adequately represents the time variability of the winter-mean NAO spatial pattern. Moreover, it correlates well ($r = 0.95$) with PC1 of the NAM (Thompson and Wallace, 2000). These results emphasise that the NAO and NAM reflect essentially the same mode of tropospheric variability. The spectrum in (c) of the winter-mean NAO index (middle panel of [b]) is slightly red, and the major conclusion is that there is no preferred time scale of NAO variability. However, the spectral peak between 6 and 9 years may be important, as time series of climate variables related to the NAO do show peaks in the decadal range of the spectrum (Da Costa and Colin de Verdier, 2004).

During the winter season, the NAO accounts for more than one-third of the total variance in sea level pressure over the North Atlantic. In the so-called positive phase, higher-than-normal surface pressures south of 55°N combine with a broad region of anomalously low pressure throughout the Arctic to enhance the climatological meridional pressure gradient. The largest amplitude anomalies occur in the vicinity of Iceland and across the Iberian Peninsula. The positive phase of the NAO is associated with stronger-than-average surface westerlies across the middle latitudes of the Atlantic onto Europe, with anomalous southerly flow over the eastern United States and anomalous northerly flow across the Canadian Arctic and the Mediterranean (Hurrell and Deser, 2010).

In summary, the NAO is an important phenomenon in the NH winter climate. Although there appears to be no preferred time scale of variability and the time series in Fig. 7.4b are too short to demonstrate significant decadal-interdecadal variability, there is definitely a preferred pattern in the Atlantic SLP anomalies, which also shows up at synoptical time scale, from a few days to several weeks. One of the most intriguing questions arising from the results is which physical processes are responsible for the NAO and hence control the low-frequency variability in the North Atlantic midlatitude winter atmosphere.

7.2 Minimal model

It is remarkable that a barotropic quasi-geostrophic model, with appropriate boundary conditions (orography) when properly forced, is able to display one of the main properties of the NAO variability, that is, its spatial pattern. The dimensionless equations

for this model can be written in streamfunction ψ and relative vorticity ζ (vertical component of the vorticity vector) formulation as (Selten, 1995)

$$\frac{\partial \zeta}{\partial t} + \mathcal{J}(\psi, \zeta + f + h) = F + D(\zeta), \quad (7.1a)$$

$$\zeta = \nabla^2 \psi. \quad (7.1b)$$

The equations have been nondimensionalised using the radius of the Earth as unit of length and the inverse of its angular velocity as unit of time. The quantity $\mathcal{J}(a, b)$ is the Jacobi operator, which, with longitude ϕ and latitude θ , is given by (with $\mu = \sin \theta$)

$$\mathcal{J}(a, b) = \frac{\partial a}{\partial \phi} \frac{\partial b}{\partial \mu} - \frac{\partial a}{\partial \mu} \frac{\partial b}{\partial \phi}. \quad (7.2)$$

Furthermore, F represents the forcing of the flow, D represents the friction (or damping) of the flow, $f = \sin \theta$ is the Coriolis parameter and h represents a prescribed orography.

In Selten (1995), realistic orography h is used and the damping is formulated as

$$D(\zeta) = k_1 \zeta + k_2 \nabla^3 \zeta, \quad (7.3)$$

where k_1 measures the strength of the Ekman damping and k_2 that of a scale-selective damping. The forcing is derived from the 500-hPa winter mean values of streamfunction ψ_{cl} and vorticity ζ_{cl} and a component of the transient eddy forcing based on 10-day running mean (winter) anomalies ψ' and ζ' , that is,

$$F = \mathcal{J}(\psi_{cl}, \zeta_{cl} + f + h) - D(\zeta_{cl}) + \overline{\mathcal{J}(\psi', \zeta')}, \quad (7.4)$$

where the overbar indicates a time average; hence the forcing is time-independent.

Spectral truncations of this model are often used (Selten, 1995) where the equation (7.1) in spherical coordinates is projected onto spherical harmonics and triangularly truncated at wave number 21. More specifically, ψ is expanded as

$$\psi(\phi, \mu, t) = \sum_{n=1}^N \sum_{m=-n}^n \psi_{n,m}(t) Y_{n,m}(\phi, \mu), \quad (7.5)$$

where $m + n$ is odd in the inner summation and the $Y_{n,m}$ are the spherical harmonics. The latter are meridionally bounded eigenfunctions of the problem

$$\nabla^2 Y_{n,m} = -n(n+1) Y_{n,m}, \quad (7.6)$$

with periodic boundary conditions in zonal direction. The expansion (7.5) is substituted into the equation (7.1), and the residual is projected on the functions $Y_{n,m}$. This gives a set of ordinary differential equations for the coefficients $\psi_{n,m}$.

In Legras and Ghil (1985), a spectrally truncated model with $N = 9$ in (7.5) of the spherical barotropic vorticity equation is studied. The results of this model are

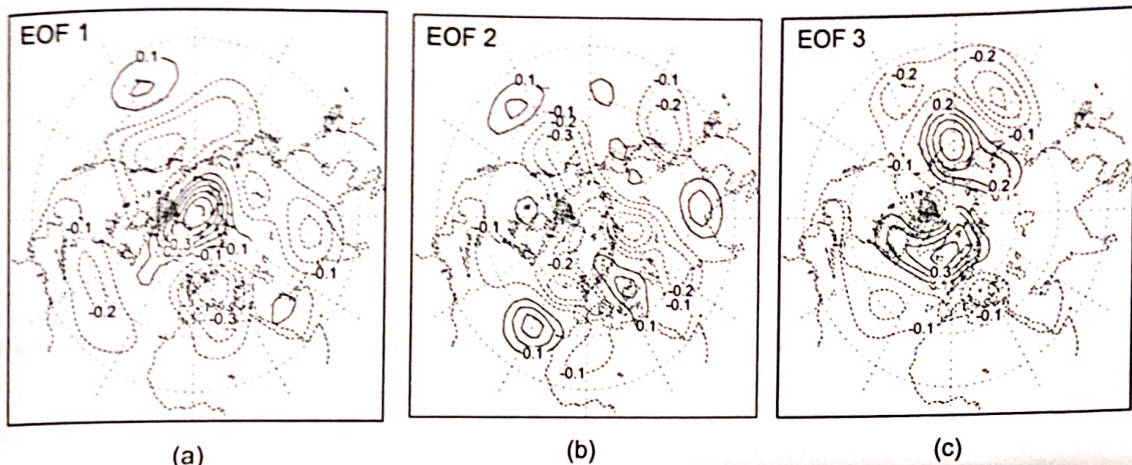


Figure 7.5 (a–c) EOF1–EOF3 calculated from a 200-yr data set produced by the T21 barotropic model. The kinetic energy norm was used for the calculation of the EOF as a measure of the variance of ψ (figure from Crommelin, 2003).

extensively discussed in Sections 6.4 and 6.5 of Ghil and Childress (1987), and particular aspects of the behavior are further investigated in Jin and Ghil (1990) and Strong et al. (1995).

In Crommelin (2003), several 200-year simulations were performed with the so-called T21 ($N = 21$ in [7.5]) version of the model of Selten (1995). The damping coefficient k_1 in (7.3) corresponds to a damping time scale of 15 days, and the scale selective damping k_2 is such that largest wave numbers are damped on a time scale of 3 days. The patterns of the first three EOFs of ψ are shown in Fig. 7.5, which explain 18.3%, 9.8% and 6.8% of the total kinetic energy in the flow. The first EOF has a similar pattern as that of the Northern Annular Mode (or Arctic Oscillation) associated with the strength of the polar vortex. The second EOF shows successive positive and negative anomalies over Western Europe. The third EOF shows a strong dipole character over the North Atlantic and resembles the pattern of the NAO.

A limited view of the probability density function (PDF) was obtained by projecting the full data set onto the PC1-PC2 plane. The result is shown as the contour plot in Fig. 7.6a, which reveals a bimodal structure with two maxima MAX1 and MAX2. The 500-hPa geopotential height anomaly patterns Z_{500} are shown in Fig. 7.6c–d. The flow pattern of MAX1 represents a situation of intensified zonal flow, and the pattern of MAX2 shows a blocked flow over Europe. The PDF-maxima MAX1 and MAX2 can be interpreted as flow regimes and the transitions between them (Fig. 7.6b) as so-called vacillatory behavior.

7.3 Variability in conceptual models

To answer the question of why the PDF in the previous section is bimodal and what processes drive the transitions between the states MAX1 and MAX2, so-called

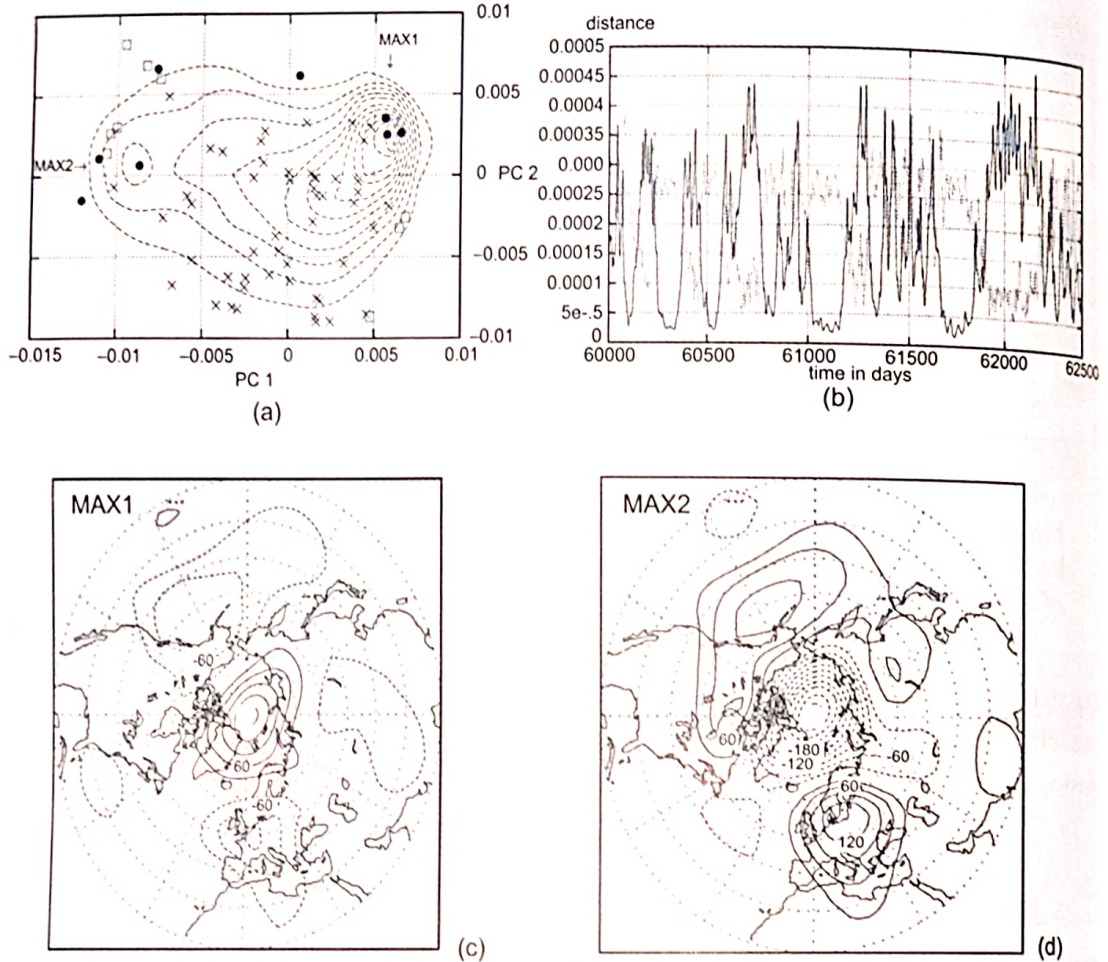


Figure 7.6 (a) Contour plot of the probability density function in the PC1-PC2 space. (b) Distances to two maxima MAX1 (solid) and MAX2 (dotted) during a data segment of 2,500 days. Distances are given as differences in turbulent kinetic energy; horizontal axis denotes time in days. (c-d) Patterns of the Z_{500} anomalies (contour interval 30 m) corresponding to the maxima of the PDF (figure from Crommelin, 2003).

reduced models have been used. Although the number of degrees of freedom d of the T21 truncated model in the previous section is not large ($d = 231$), an even further reduction allows for an easier mechanistic analysis (De Swart, 1989).

7.3.1 A six-mode model

In many studies with reduced models, the geometry is idealized to a zonal channel of width πbL and length $2\pi L$ on a midlatitude β plane with Coriolis parameter $f = f_0 + \beta_0 y$. In Cartesian coordinates, the dimensional equations are

$$\frac{\partial \zeta}{\partial t} + \mathcal{J}\left(\psi, \zeta + \beta_0 y + \frac{f_0}{H} h\right) = F + D(\zeta), \quad (7.7a)$$

$$\zeta = \nabla^2 \psi, \quad (7.7b)$$

where H is the thickness of the layer and

$$\mathcal{J}(a, b) = \frac{\partial a}{\partial x} \frac{\partial b}{\partial y} - \frac{\partial b}{\partial x} \frac{\partial a}{\partial y}.$$

In Crommelin et al. (2004), the dissipation and forcing are taken as

$$F = k\zeta^*; D = -k\zeta, \quad (7.8)$$

where ζ^* is a prescribed function and k represents Ekman damping. When (7.7) is nondimensionalised using scales $1/f_0$ for time, L for length x and y , and $L^2 f_0$ for the streamfunction, f_0 for vorticity and H for topography, the dimensionless equation for ψ becomes

$$N(\psi, h, \psi^*) = \frac{\partial \nabla^2 \psi}{\partial t} + \mathcal{J}(\psi, \nabla^2 \psi + \beta y + \gamma h) + C \nabla^2 (\psi - \psi^*) = 0 \quad (7.9)$$

with $\beta = \beta_0 L/f_0$ and $C = k/f_0$, and the dimensionless parameter γ is introduced as a scaling factor of the orography. From now on, all dependent quantities are dimensionless in this subsection.

The set of basis functions used to derive the low-order model is chosen as the eigenfunctions of the Laplace equation on the domain $[0, 2\pi] \times [0, \pi b]$, that is,

$$\nabla^2 \phi_{n,m} = -\lambda_{n,m} \phi_{n,m}, \quad (7.10)$$

which satisfy periodic boundary conditions on the x direction and $\partial \phi_{n,m} / \partial x = 0$ at the channel walls $y = 0$ and $y = \pi b$. These eigenfunctions, when chosen to be orthonormal, are given by

$$\phi_{0,m}(y) = \sqrt{2} \cos \frac{my}{b}, \quad (7.11a)$$

$$\phi_{n,m}(x, y) = \sqrt{2} e^{inx} \sin \frac{my}{b}. \quad (7.11b)$$

The streamfunction ψ , the topography h and the forcing field ψ^* are now expanded as

$$(\psi, h, \psi^*) = \sum_{n,m} (\psi_{n,m}(t), h_{n,m}(t), \psi_{n,m}^*(t)) \phi_{n,m}. \quad (7.12)$$

These expansions are substituted into the equation (7.9) and projected using a Galerkin method, that is, for every n, m

$$\langle N(\psi, h, \psi_*), \psi_{n,m} \rangle = \frac{1}{2\pi^2 b} \int_0^{2\pi} \int_0^{\pi b} N(\psi, h, \psi_*) \psi_{n,m} dx dy = 0, \quad (7.13)$$

where $\langle \cdot, \cdot \rangle$ is the inner product and N given by (7.9).

Next, the topography and forcing are chosen as

$$h(x, y) = \cos x \sin \frac{y}{b}; \psi^*(x, y) = \Phi(y), \quad (7.14)$$

with $\Phi(y)$ a given function. This implies that $h_{1,1} = h_{-1,1} = 1/(2\sqrt{2})$ and all other $h_{n,m}$ are zero. Furthermore, only modes $\phi_{0,1}, \phi_{0,2}, \phi_{1,1}, \phi_{-1,1}, \phi_{1,2}$ and $\phi_{-1,2}$ are considered. With

$$\begin{aligned}x_1 &= \frac{1}{b}\psi_{0,1}; \quad x_2 = \frac{1}{\sqrt{2}b}(\psi_{1,1} + \psi_{-1,1}); \quad x_3 = \frac{i}{\sqrt{2}b}(\psi_{1,1} - \psi_{-1,1}) \\x_4 &= \frac{1}{b}\psi_{0,2}; \quad x_5 = \frac{1}{\sqrt{2}b}(\psi_{1,2} + \psi_{-1,2}); \quad x_6 = \frac{i}{\sqrt{2}b}(\psi_{1,2} - \psi_{-1,2}),\end{aligned}$$

the projected equations (for $n = -1, 0, 1, m = 0, 2$) become

$$\frac{dx_1}{dt} = \tilde{\gamma}_1 x_3 - C(x_1 - x_1^*), \quad (7.15a)$$

$$\frac{dx_2}{dt} = -(\alpha_1 x_1 - \beta_1) x_3 - C x_2 - \delta_1 x_4 x_6, \quad (7.15b)$$

$$\frac{dx_3}{dt} = (\alpha_1 x_1 - \beta_1) x_2 - \gamma_1 x_1 - C x_3 + \delta_1 x_4 x_5, \quad (7.15c)$$

$$\frac{dx_4}{dt} = \tilde{\gamma}_2 x_6 - C(x_4 - x_4^*) + \epsilon(x_2 x_6 - x_3 x_5), \quad (7.15d)$$

$$\frac{dx_5}{dt} = -(\alpha_2 x_1 - \beta_2) x_6 - C x_5 - \delta_2 x_4 x_3, \quad (7.15e)$$

$$\frac{dx_6}{dt} = (\alpha_2 x_1 - \beta_2) x_5 - \gamma_2 x_4 - C x_6 + \delta_2 x_4 x_3, \quad (7.15f)$$

with chosen coefficients $x_4^* = r x_1^*$ (note that x_1^* and x_4^* are the only two nonzero coefficients when ψ^* is only a function of y) and

$$\begin{aligned}\alpha_m &= \frac{8\sqrt{2}}{\pi} \frac{m^2}{4m^2 - 1} \frac{b^2 + m^2 - 1}{b^2 + m^2}; \quad \beta_m = \frac{\beta b^2}{b^2 + m^2}, \\ \gamma_m &= \gamma \frac{4m^3}{4m^2 - 1} \frac{\sqrt{2}b}{\pi(b^2 + m^2)}; \quad \delta_m = \frac{64\sqrt{2}}{15\pi} \frac{b^2 - m^2 + 1}{b^2 + m^2}, \\ \tilde{\gamma}_m &= \gamma \frac{4m}{4m^2 - 1} \frac{\sqrt{2}b}{\pi}; \quad \epsilon = \frac{16\sqrt{2}}{5\pi},\end{aligned}$$

for $m = 0, 2$. In these equations, the terms with the δ_m and ϵ describe the nonlinear triad interactions between $\phi_{0,2}$ and the $\phi_{1,1}$ and $\phi_{2,2}$ modes. The terms with β represent the advection of planetary vorticity, the ones with α represent the advection of the modes by the zonal flow and the terms with γ represent the effect of topography.

In Crommelin (2004), the parameters $\beta = 1.25$, $b = 0.5$, $C = 0.1$ and $\gamma = 1.0$ are taken fixed, and either the parameter r or x_1^* is used as a control parameter. For $r = -0.4$, the bifurcation diagram of the model (showing x_1 versus x_1^*) is shown in Fig. 7.7. There are two saddle-node bifurcations (labelled as sn1 and sn2) that induce a regime of multiple steady states. The three equilibria at $x_1^* = 6.0$, for which

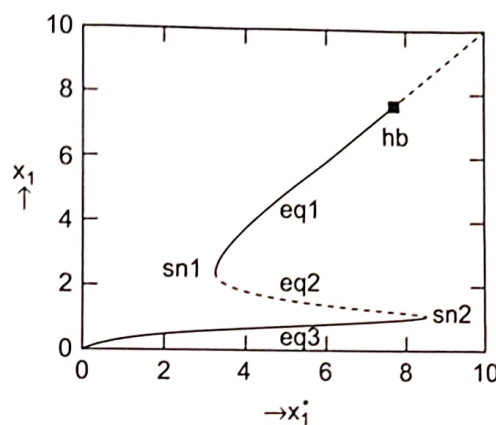


Figure 7.7 Bifurcation diagram showing x_1 versus x_1^* of the reduced atmospheric model (7.15) with $r = -0.4$. The drawn (dashed) curve represents stable (unstable) steady solutions (figure from Crommelin et al., 2004).

streamfunction patterns are shown in Fig. 7.8, are associated with three different ways in which the advection of potential vorticity and the vortex stretching caused by flow over topography can balance.

The stable flow eq1 in Fig. 7.8 is the so-called zonal flow, and the stable equilibrium eq3 in Fig. 7.8 is the blocked flow. The third equilibrium flow (eq2 in Fig. 7.8) is

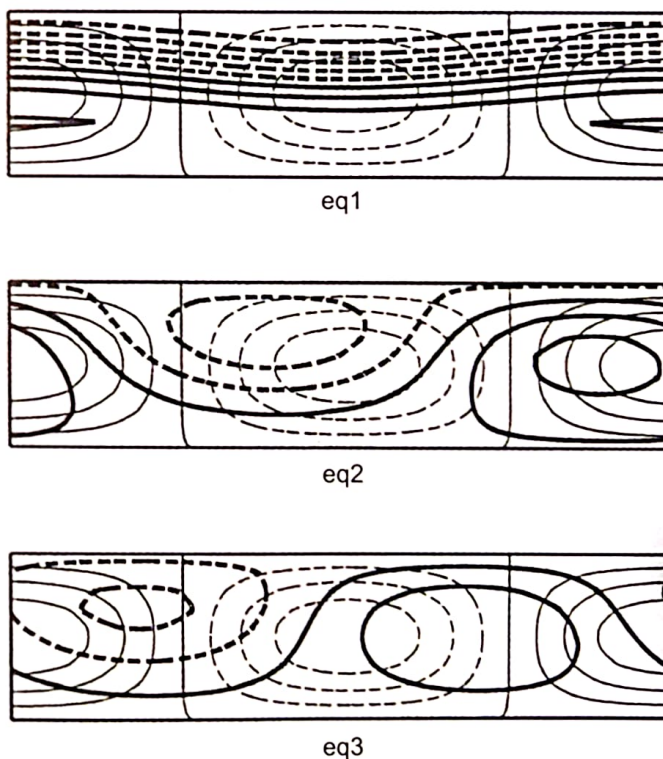


Figure 7.8 Solutions for the streamfunction ψ (thick curves) of the reduced atmospheric model (7.15) with $r = -0.4$ and $x_1^* = 6.0$. The contour levels of the topography are shown as the thinner curves (figure from Crommelin et al., 2004).

unstable (cf. the dashed curve in Fig. 7.7). For larger values of x_1^* , the zonal flow state becomes unstable through a Hopf bifurcation, which, as we learned in Chapter 2, is an oscillatory instability. We now turn to the physical mechanisms of these basic instabilities.

7.3.2 Instability mechanisms

The first issue to explain is the occurrence of the saddle-node bifurcations and hence the multiple equilibrium regime. When the initial conditions are such that $x_4 = x_5 = x_6 = 0$, we see from (7.15) that these amplitudes remain zero if $x_4^* = 0$ ($r = 0$). The system of equations (7.15) then reduces to

$$\frac{dx_1}{dt} = \tilde{\gamma}_1 x_3 - C(x_1 - x_1^*), \quad (7.16a)$$

$$\frac{dx_2}{dt} = -(\alpha_1 x_1 - \beta_1) x_3 - C x_2, \quad (7.16b)$$

$$\frac{dx_3}{dt} = (\alpha_1 x_1 - \beta_1) x_2 - \gamma_1 x_1 - C x_3, \quad (7.16c)$$

which is often referred to as the Charney-DeVore model (Charney and DeVore, 1979).

The steady states of the Charney-deVore model are easily solved by introducing $\omega = \alpha_1 x_1 - \beta_1$ and solving the system (7.16b,c) for x_2 and x_3 in terms of x_1 , which gives

$$x_2 = \frac{\omega \gamma_1}{\omega^2 + C^2} x_1; \quad x_3 = -\frac{C \gamma_1}{\omega^2 + C^2} x_1. \quad (7.17)$$

Substituting the result into (7.16a) gives a third-order equation for x_1 as

$$F(x_1) = \left(\frac{\tilde{\gamma}_1 \gamma_1}{\omega^2 + C^2} + 1 \right) x_1 = x_1^*. \quad (7.18)$$

The function $F(x_1)$ is shown for several values of γ in Fig. 7.9. For small x_1^* , there is only one solution of (7.18), but as the topography height γ increases, eventually three solutions appear. From this analysis, it is clear that the modes x_4 , x_5 and x_6 in (7.15) are not needed to explain the existence of the multiple equilibria.

The linear stability analysis of a steady state $(\bar{x}_1, \bar{x}_2, \bar{x}_3)$ leads to an eigenvalue problem for the Jacobian matrix J of (7.16), which is

$$J = \begin{pmatrix} -C & 0 & \tilde{\gamma}_1 \\ -\alpha_1 \bar{x}_3 & -C & \beta_1 - \alpha_1 \bar{x}_1 \\ -\gamma_1 + \alpha_1 \bar{x}_2 & -\beta_1 + \alpha_1 \bar{x}_1 & -C \end{pmatrix}. \quad (7.19)$$

The value of $\omega(\bar{x}_1)$ is plotted versus x_1^* for $\gamma = 1$ in Fig. 7.10a, and the eigenvalues σ of (7.19) along the branches are plotted in Fig. 7.10b–c. At small \bar{x}_1 , there is one real

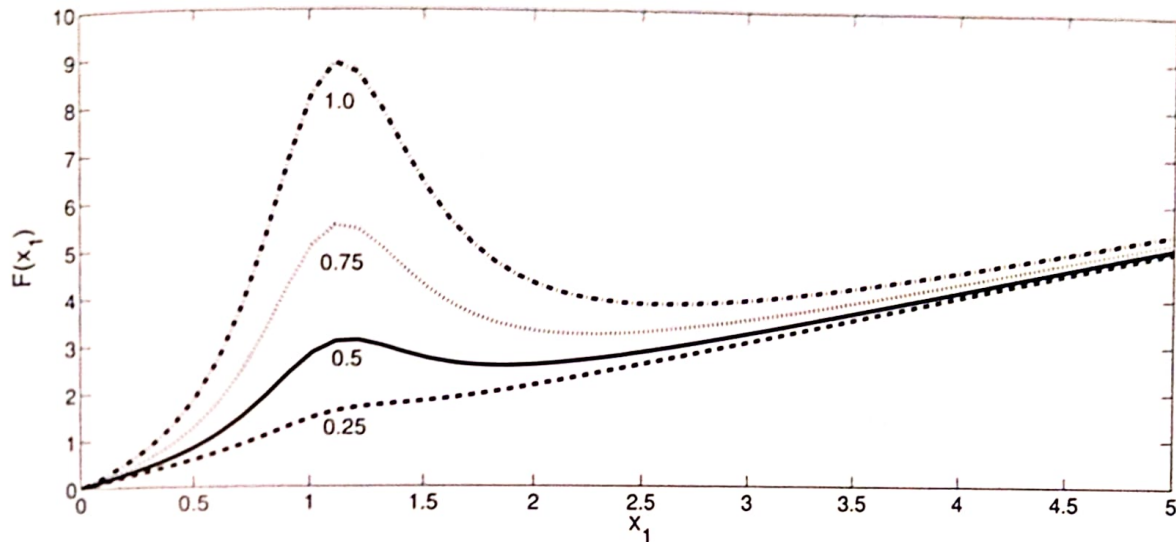


Figure 7.9 The function $F(x_1)$ in (7.18) for several values of γ .

eigenvalue σ_1 and a complex conjugate pair $\sigma_{2,3}$ (indicated by the circles and crosses in Fig. 7.10b,c), all with a negative real part. When the first saddle-node bifurcation point is approached, the value of $\omega \approx 0$ and $\sigma_1 \approx 0$, and while crossing the saddle node, the value of $\sigma_1 > 0$, whereas the real part of the pair $\sigma_{2,3} < 0$. On the unstable branch, between the saddle nodes, only $\sigma_1 > 0$, and it passes through zero again at the second saddle-node bifurcation. Hence the instability is associated with only one real eigenvalue (σ_1), whereas the oscillatory pair plays no role.

The instability mechanism associated with the real eigenvalue is called topographic instability (Charney and DeVore, 1979). The mechanism is most easily illustrated by considering the nondissipative case $C = 0$, for which the equations (7.16) reduce to

$$\frac{dx_1}{dt} = \tilde{\gamma}_1 x_3, \quad (7.20a)$$

$$\frac{dx_2}{dt} = -(\alpha_1 x_1 - \beta_1) x_3, \quad (7.20b)$$

$$\frac{dx_3}{dt} = (\alpha_1 x_1 - \beta_1) x_2 - \gamma_1 x_1. \quad (7.20c)$$

Here the steady states are given by $\bar{x}_3 = 0$ and $\bar{x}_2 = \gamma_1 \bar{x}_1 / \omega$, with $\omega = (\alpha_1 \bar{x}_1 - \beta_1)$ and \bar{x}_1 arbitrary (for example, $\bar{x}_1 = x_1^*$). Perturbations $(\tilde{x}_1, \tilde{x}_2, \tilde{x}_3)$ from these steady states satisfy the linearised equations

$$\frac{d\tilde{x}_1}{dt} = \tilde{\gamma}_1 \tilde{x}_3, \quad (7.21a)$$

$$\frac{d\tilde{x}_2}{dt} = -\omega \tilde{x}_3, \quad (7.21b)$$

$$\frac{d\tilde{x}_3}{dt} = \omega \tilde{x}_2 - (\gamma_1 - \alpha_1 \bar{x}_2) \tilde{x}_1 = \omega \tilde{x}_2 + \frac{\beta_1 \gamma_1}{\omega} \tilde{x}_1. \quad (7.21c)$$

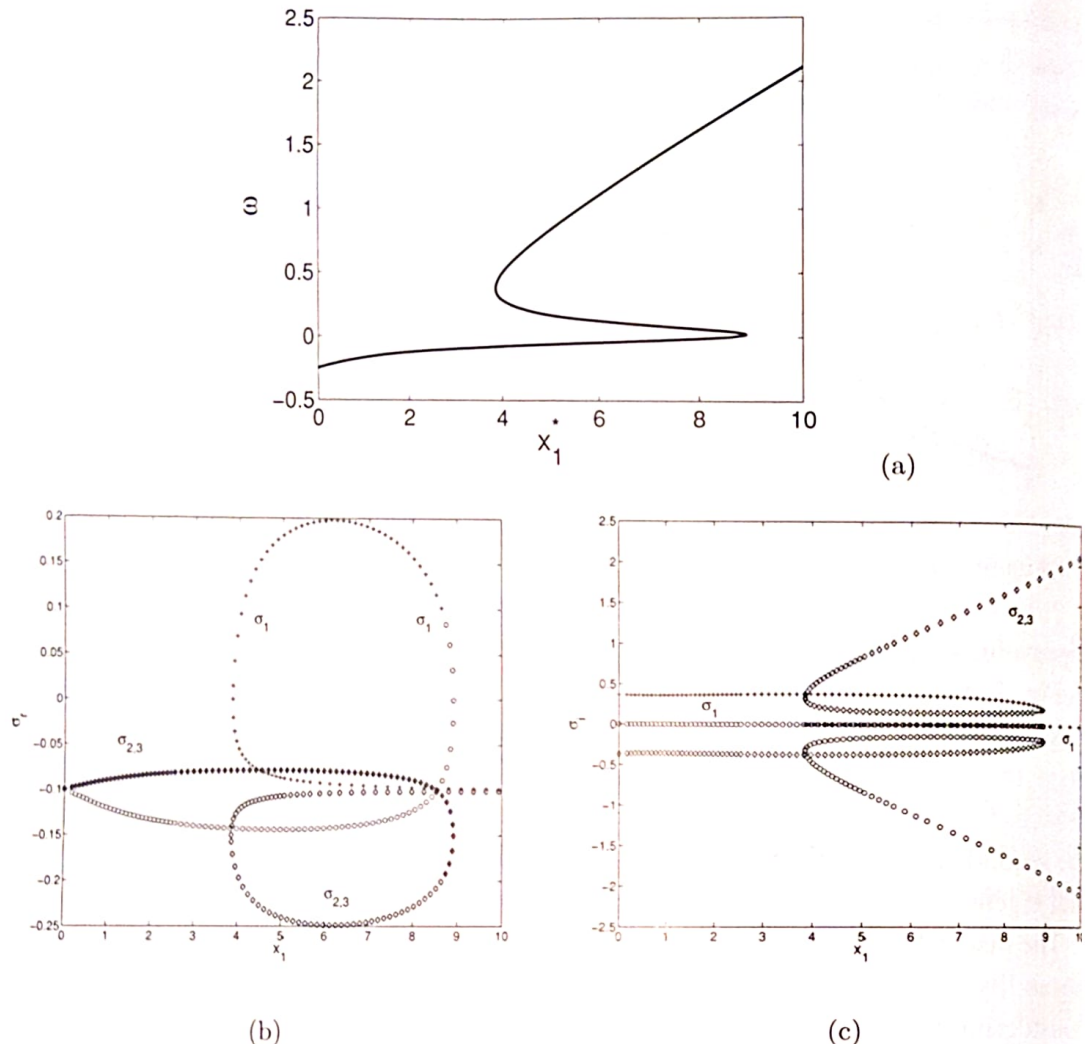


Figure 7.10 (a) Value of the parameter $\omega = \alpha x_1 - \beta_1$ along the branches of steady states when x_1^* is changed. (b) Real part σ_r of the eigenvalues of J in (7.19). (c) Imaginary part σ_i of the eigenvalues of J .

Differentiating (7.21c) to time and using (7.21a) and (7.21b) leads to

$$\frac{d^2\tilde{x}_3}{dt^2} + \left(\omega^2 - \frac{\beta_1 \tilde{\gamma}_1 \gamma_1}{\omega} \right) \tilde{x}_3 = 0, \quad (7.22)$$

and hence exponential growth will occur when $\omega^2 - \beta_1 \tilde{\gamma}_1 \gamma_1 / \omega < 0$. The presence of the topography is essential because when $\gamma = 0$, then $\gamma_1 = \tilde{\gamma}_1 = 0$ and there is only oscillatory behaviour.

The instability mechanism is sometimes also referred to as topographic resonance because it involves a special case of parametric resonance that occurs in oscillators where the frequency varies with time according to $A \cos \omega_1 t$, giving an equation of

the form

$$\frac{d^2x}{dt^2} + \omega_0^2(1 + A \cos \omega_1 t)x = 0. \quad (7.23)$$

In this case, resonance occurs for small A and $\omega_1 = 2\omega_0/n$ for integer n . In topographic instability, $\omega_1 \approx 0$, and resonance occurs, due to the topography, with a near stationary change in frequency (Ghil and Childress, 1987).

The second instability mechanism is related to the occurrence of the Hopf bifurcation on the zonal flow solution branch in Fig. 7.7. As can be concluded from the previous analysis, such a Hopf bifurcation does not occur in the three-mode (Charney-deVore) model, and hence patterns of $\phi_{0,2}$, $\phi_{1,2}$ and $\phi_{-1,2}$ are necessary to represent the instability. This is a so-called barotropic instability, where the energy of the perturbations is extracted from the horizontal shear of the background steady state through the Reynolds' stresses. As the instability mechanism is well described in other textbooks on dynamical meteorology and oceanography (Holton, 1992; Pedlosky, 1987), we do not expand on this here in more detail.

7.3.3 Low-frequency variability

When a trajectory is computed in the original six-mode model (7.15) with $\gamma = 0.2$, $x_1^* = 0.95$ and $r = -0.801$, the result of Fig. 7.11a is found, with the spatial patterns of the flows labelled eq1 and eq2,3 shown in Fig. 7.11b. Clearly, there is low-frequency variability, where the pattern seems to make excursions between a pattern of a zonal flow and a blocked flow.

The origin of the low-frequency variability in this model is due to homoclinic and heteroclinic bifurcations (cf. Section 2.5.1). These arise here through a so-called fold-Hopf bifurcation. The value of x_1^* at the Hopf bifurcation and the saddle-node bifurcations in Fig. 7.7 depend on other parameter values, for example, r and γ . The position of the saddle-node sn1 does not depend much on r (which is the forcing of the ϕ_{02} pattern), whereas the Hopf bifurcation will shift to smaller values of x_1^* when r becomes more negative.

For the case $\gamma = 0.2$, this can be seen in three bifurcation diagrams (where x_1 is plotted versus x_1^*) that are plotted for different values of r in Fig. 7.12. The bifurcation diagram for $r = -0.7$ is qualitatively similar to that in Fig. 7.7. Near $r = -0.8$, which is the case considered in Fig. 7.11, the saddle-node sn1 and the Hopf bifurcation H have nearly merged. For $r = -0.9$, the Hopf bifurcation is already located on the unstable branch of steady solutions.

From Fig. 7.12, it can be concluded that there exists a value of r such that the saddle-node sn1 and the Hopf bifurcation coalesce (occur at the same value of x_1^*). This is the location of the fold-Hopf bifurcation. The different possibilities of the behaviour of trajectories near the fold-Hopf bifurcation can be found, for example, in

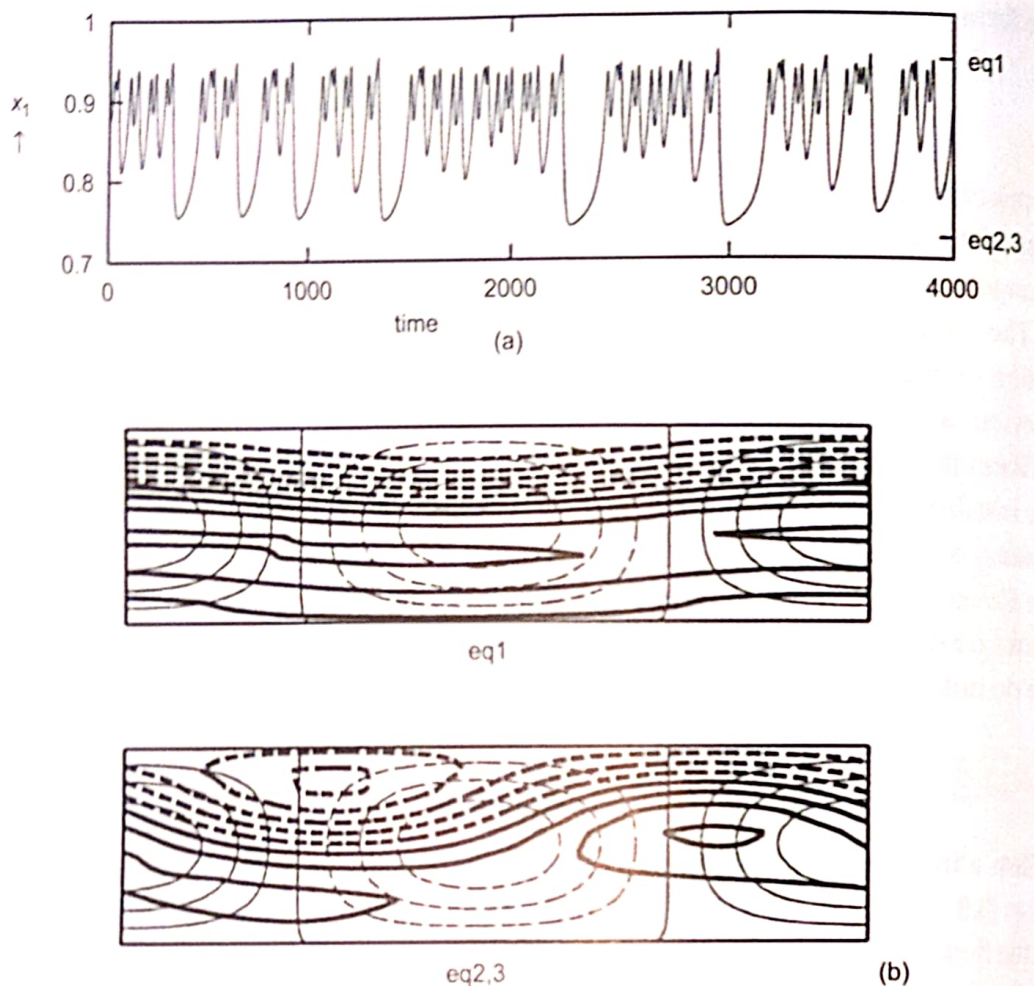


Figure 7.11 (a) Trajectory of the six-mode model with $\gamma = 0.2$, $x_1^* = 0.95$ and $r = -0.801$. (b) Streamfunction patterns of the states eq1 and eq2,3 in (a); figure from Crommelin et al. (2004).

detail in Kuznetsov (1995). As the Hopf bifurcation is supercritical, there is only one possibility, and the phase portraits are shown in Fig. 7.13. Here ρ_1 and ρ_2 are the control parameters, which can be thought of as r and x_1^* , respectively. In the middle figure, the path of the Hopf bifurcations (hb) intersects the path of the saddle node (sn).

To interpret the diagrams in Fig. 7.13, consider a fixed value of $\rho_2 < 0$ (fixed r) and a decreasing ρ_1 (increasing x_1^*). This is similar to investigating the behaviour locally near the $sn1 - H$ branch for $r = -0.7$ in Fig. 7.12 with increasing x_1^* . For x_1^* smaller than the value of $sn1$, locally no steady states exist, and there are no periodic orbits (of course, there is a steady state far away, but note that this is a local analysis), and hence this is regime a in Fig. 7.12. When the saddle node (sn) is passed (at $\rho_1 = 0$), two new equilibria are created, of which one is stable and one is unstable. These equilibria are sketched at the dots in regime f, where the upper one is attracting all trajectories (and hence this is the stable one) and the lower one is unstable. At slightly more negative ρ_1 (slightly larger x_1^*), the Hopf bifurcation H (hb in Fig. 7.12)

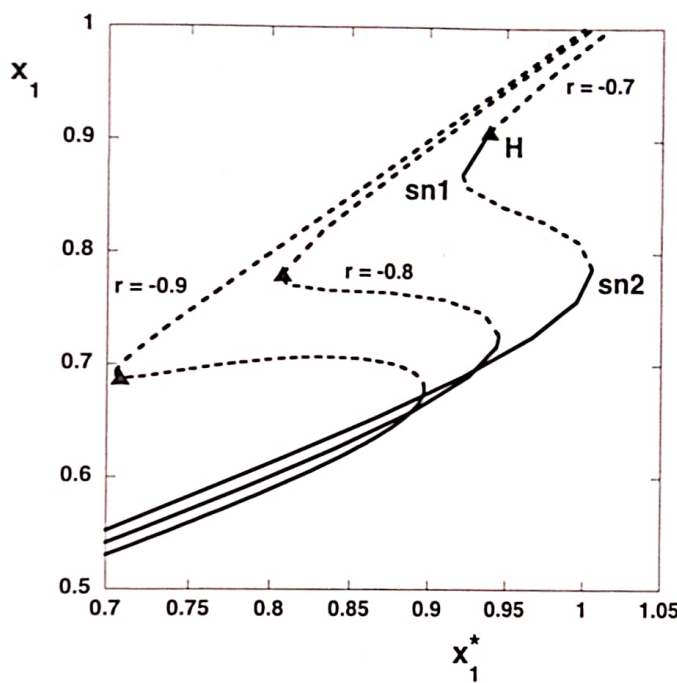


Figure 7.12 Bifurcation diagrams of the six-mode model with $\gamma = 0.2$ and different values of r . Solid (dashed) branches indicate stable (unstable) solutions, and the Hopf bifurcation (H) is indicated by a triangle.

is found, and the upper fixed point in regime f becomes unstable and a periodic orbit exists, which is case d. The amplitude of the periodic orbit becomes eventually so large that it touches both equilibria, and hence a heteroclinic connection (hc) is established. The case $r = -0.9$ corresponds to the case $\rho_2 > 0$, where all steady states and periodic orbits are unstable (cases b and c). As we have seen in Section 2.5.1, homoclinic and heteroclinic connections are associated with irregular dynamics and with trajectories displaying variability at low frequency. The existence of these heteroclinic connections explains the behaviour (low-frequency switching between two equilibria) displayed in Fig. 7.11.

7.4 Beyond conceptual models

Although the reduced (low-order) models have been very instructive for illuminating mechanisms of variability in atmospheric midlatitude flows, it is not at all clear whether the mechanisms identified are responsible for low-frequency behaviour in the minimal model (Section 7.2), for models higher up in the hierarchy as described in Chapter 6, and observations.

7.4.1 Barotropic quasi-geostrophic models

In Fig. 7.6a, the crosses, dots and squares indicate steady states of the minimal model (7.1), where the markers distinguish the degree of projection of these steady states

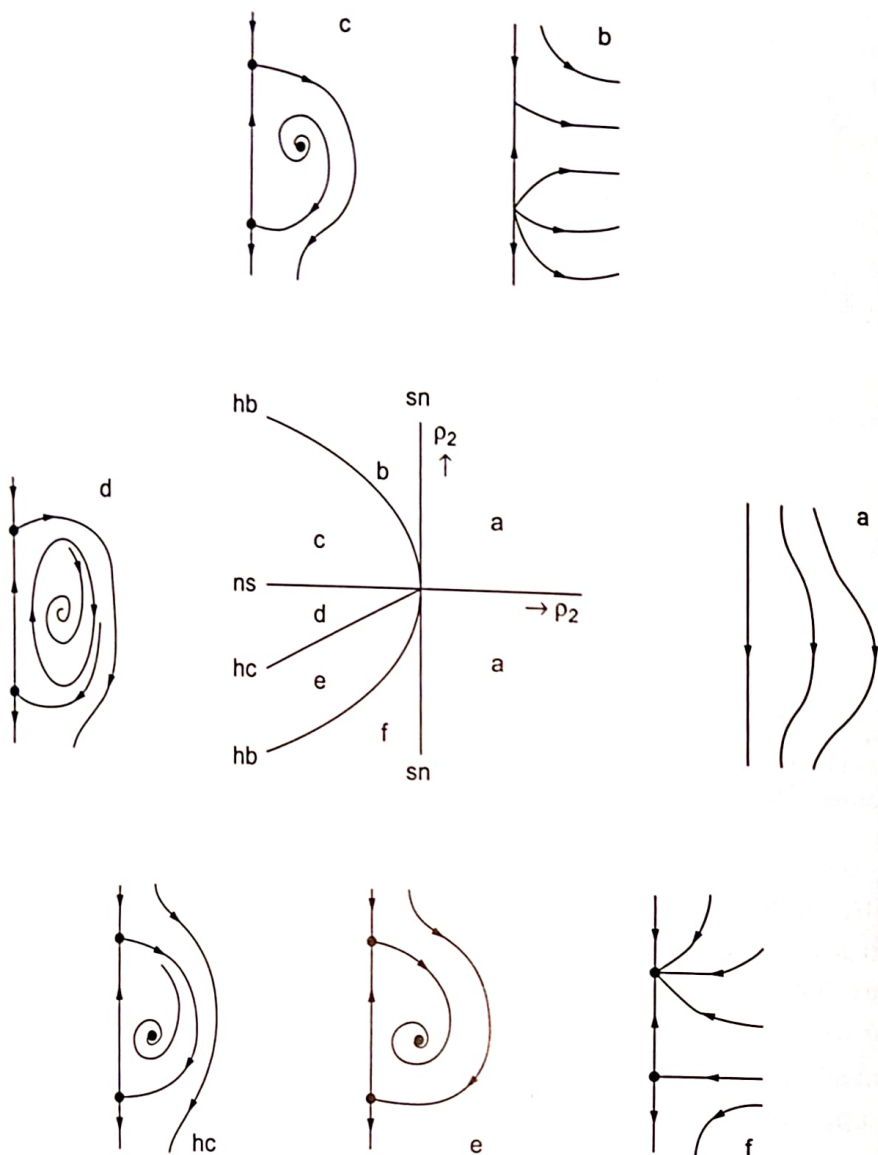


Figure 7.13 Different behaviour (phase-plane pictures) near the fold-Hopf point in a two-parameter (ρ_1, ρ_2) plane (figure from Crommelin et al., 2004).

onto the leading two EOFs; at least sixty-eight fixed points were found (Crommelin, 2003). This does not motivate us to totally clarify the bifurcation behaviour of these models, and one, moreover, wonders how the specific truncation affects the number of fixed points.

Indications for the existence of heteroclinic connections in the minimal model were found in Crommelin (2003). In Fig. 7.14a the projection of trajectories starting near MAX1 (near steady-state A) in the PC1–PC3 plane shows that these end up near B, whereas during the transition, the sign of PC3 is negative. In contrast, in Fig. 7.14b, trajectories started near MAX2 (steady-state B) end up near A, but the sign of PC3 is positive. Using an optimisation technique, approximations of heteroclinic orbits are

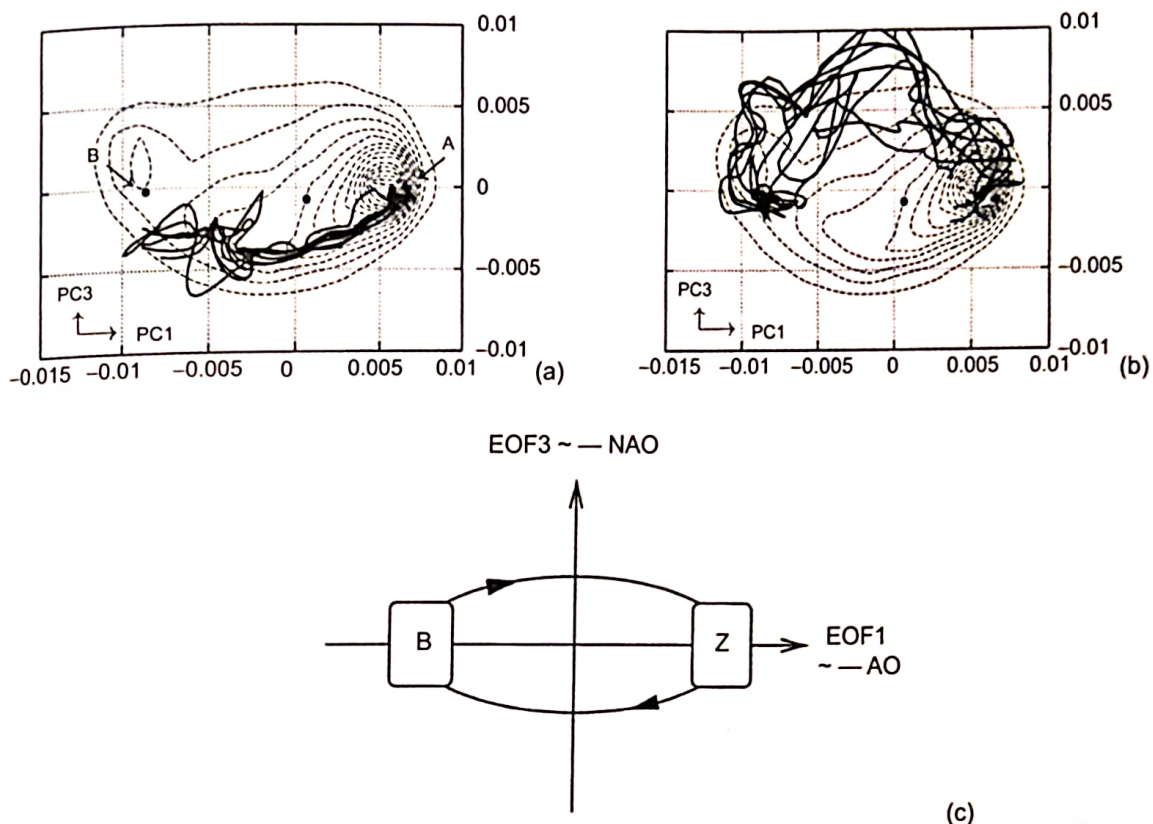


Figure 7.14 Projection of transition orbits in the PC1–PC3 plane. (a) Orbits starting close to steady state A near MAX1. (b) Orbits starting close to steady state B near MAX2. Also shown are the contours (dashed) of the probability density function of the 200-yr data set. (c) Schematic representation of the interrelationships of regime behavior, NAO and AO, as emerging from the barotropic model. Here, B denotes the blocked regime; Z is the zonal regime. Negative PC1 corresponds to a stronger polar vortex (positive AO phase); negative PC3 corresponds to the positive NAO phase (figure from Crommelin, 2003).

computed in Crommelin (2003), providing strong support for the existence of these orbits. These orbits play an important role in the transition between zonal (Z) and blocked regimes (B) of the atmospheric flow in this model.

From these results, a highly simplified, schematic picture of the dynamics of regime behaviour between NAO and AO (Fig. 7.14c) was suggested (Crommelin et al. 2003). A negative value of PC1 corresponds to a stronger polar vortex (positive AO phase), whereas a negative value of PC3 corresponds to a positive NAO phase. Starting in the zonal regime, which shows a polar vortex that is weaker than average, the model evolves via a positive NAO phase to the blocked regime. The blocked regime is characterised by a blocking over Europe and, on a larger scale, a strong polar vortex. Leaving the blocked regime, the block persists for a while but shifts to the west, to the North Atlantic. This transition phase thereby gets the features of a negative NAO phase, and finally, the model atmosphere is back in the zonal regime.

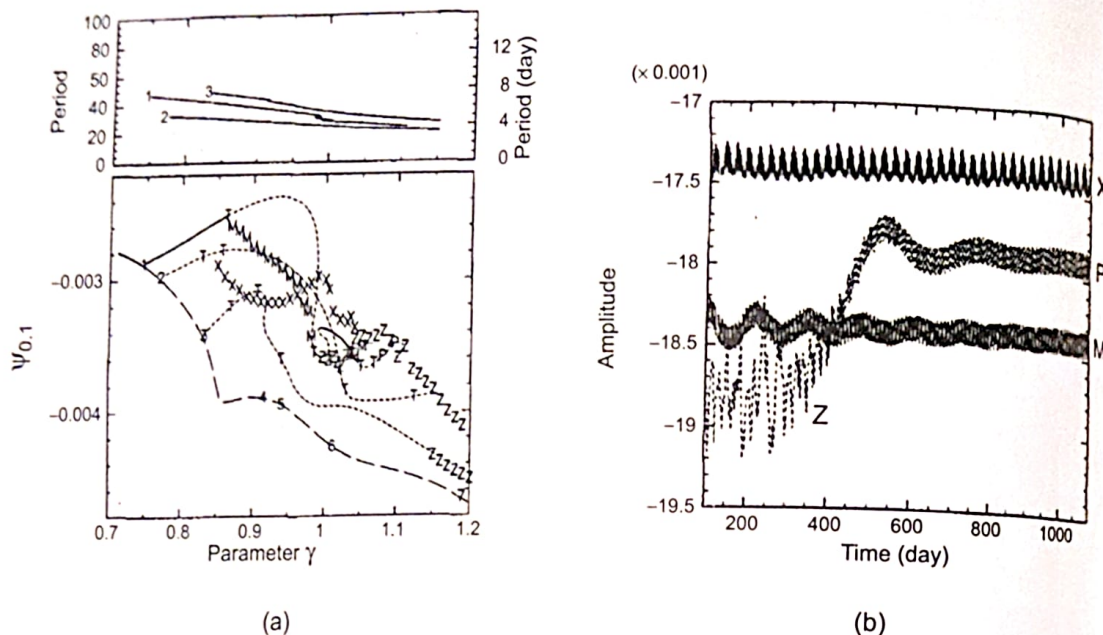


Figure 7.15 (a) Bifurcation diagram of the two-layer linear balance quasi-geostrophic model as in Itoh and Kimoto (1996). The lower branch represents steady states (drawn: stable; dashed: unstable). From the numerals, periodic solutions branch from the steady states (drawn: stable; dotted: unstable). The points labelled T are Neimark-Sacker bifurcations, and the labels X, M, P and Z point to particular time-dependent states. (b) Time variation of $\psi_{0,1}$ for $\gamma = 1$ for several different trajectories, illustrating the states X, P, M and Z.

7.4.2 Baroclinic quasi-geostrophic models

In Mukougawa (1988), a low-order truncation of a two-layer quasi-geostrophic model (having 28 degrees of freedom) in a β channel is analysed. Apart from real steady states, so-called quasi-stationary states, shown to be characterised by a small-phase space velocity, are also investigated. Again, many steady and quasi-stationary states as well as Hopf bifurcations were found.

An extension of the Legras and Ghil (1985) study for a two-level linear balance quasi-geostrophic model was presented in Itoh and Kimoto (1996). A spherical harmonic truncation was applied of the governing equations, leading to a dynamical system of 240 degrees of freedom. As control parameter, the equator to pole temperature gradient parameter γ was chosen, with $\gamma = 1$ corresponding to a realistic value. The bifurcation diagram was computed using the AUTO (Doedel, 1980) code, and details on the time-dependent behaviour were determined with many transient model simulations.

The bifurcation diagram, showing the amplitude of one of the streamfunction mode components $\psi_{0,1}$ versus γ , is plotted in Fig. 7.15a. The steady state, which is stable at a small value of γ , destabilises through a sequence of Hopf bifurcations where periodic solutions appear. The periods of the first three solutions are shown to be in

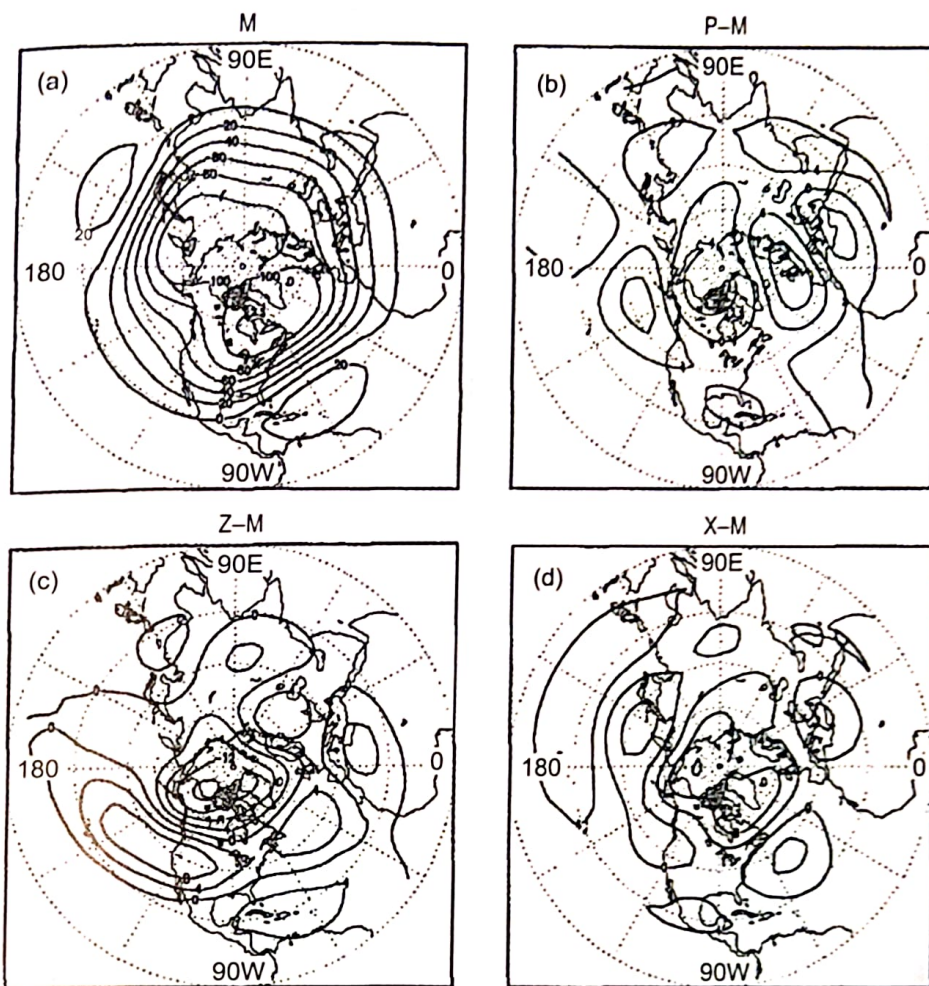


Figure 7.16 Time-mean upper level streamfunction for (a) state M , (b) state P , (c) state Z and (d) state X . Only (a) is the total field (contour interval $20 \times 10^6 \text{ m}^2 \text{s}^{-1}$) and deviations from (a) (contour interval $4 \times 10^6 \text{ m}^2 \text{s}^{-1}$) are plotted in (b–d); figure from Itoh and Kimoto (1996).

the range of 4–10 days (upper panel of Fig. 7.15). The periodic solutions destabilise through Neimark-Sacker (Section 2.4) bifurcations, leading to quasi-periodic and chaotic solutions. Several of the time-dependent equilibrium solutions are labelled in Fig. 7.15a, and trajectories computed are shown in Fig. 7.15b. Clearly X , M and P are equilibrium solutions, whereas the state Z appears as a transient state, which can persist for about 400 days.

The time-mean patterns of upper-level streamfunction for the state M and the differences between M and X , P and Z are shown in Fig. 7.16. The difference patterns $P-M$, $Z-M$ and $X-M$ are characterised either by wave trains passing near the North Pole (Fig. 7.16b,d) or by a north-south dipolar pattern (Fig. 7.16c). It was shown that when noise is applied to the heat flux in the model, a trajectory may iterate over the remains of the attractors (e.g., X , Z and P) in what Itoh and Kimoto (1996)

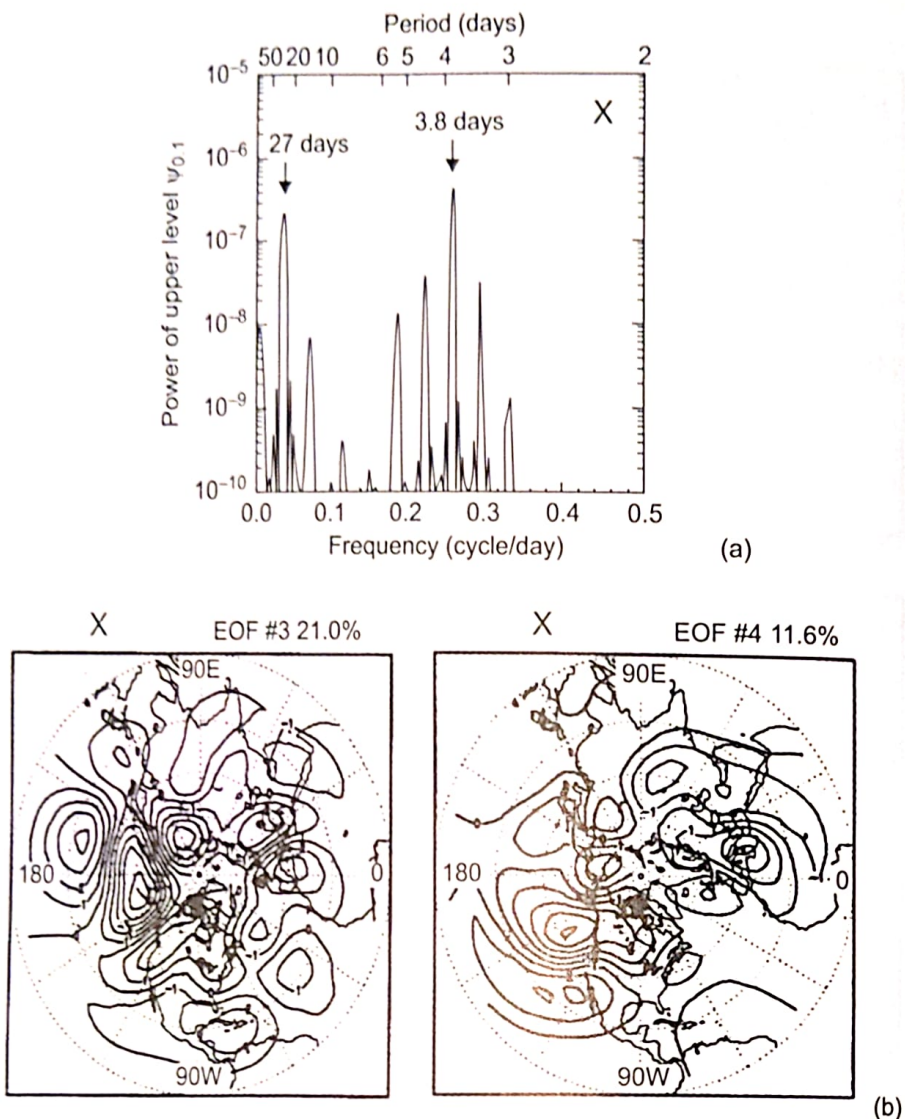


Figure 7.17 (a) Fourier spectrum of the trajectory around the equilibrium state X . (b) Patterns of the EOF3 and EOF4 showing the pattern of the low-frequency oscillation (figure from Itoh and Kimoto, 1996).

call ‘chaotic itinerancy’. In Selten and Branstator (2004), using a T21 three-level quasi-geostrophic model, different equilibrium states are also found, which correspond to the so-called Pacific North American (PNA) and the Northern Annular Mode (NAM) pattern. Support is found for the existence of an unstable period that connects the different regimes, and it is suggested to be a remnant of a heteroclinic connection.

As can be seen in Fig. 7.15b, the trajectories around the states Z and X clearly display low-frequency variability. The spectrum of X is shown in Fig. 7.17a. The short-term dominant variability (of 3.8 days) is associated with baroclinic instability. The low-frequency variability is associated with the patterns of EOF3 and EOF4 (shown in Fig. 7.17b).

7.4.3 Baroclinic shallow-water models

The first study to use a two-layer shallow-water model was Keppenne et al. (2000). No detailed bifurcation diagrams were provided, but the focus was on the intraseasonal variability in the atmospheric angular momentum in the model. Spectral analysis of a 100-year long time series led to the identification of oscillations with 35–40 days and 65–70 days. The 70-day variability was not found so far in the quasi-geostrophic models and so was suggested to involve the ageostrophic flow component. The topography was found to be central in all the intraseasonal oscillations found.

In Sterk et al. (2010), a highly truncated version of the two-layer shallow water model in a β -plane channel was constructed. In each layer the velocity field (u, v) is two-dimensional. The thickness h of each layer is variable, which is the only three-dimensional aspect of this model. With the constants H_1 and H_2 denoting the mean thickness of each layer, and the fields η'_1 and η'_2 the deviations from the mean thickness, the thickness fields of the two layers are given by

$$h'_1 = H_1 + \eta'_1 - \eta'_2, \quad (7.24a)$$

$$h'_2 = H_2 + \eta'_2 - h'_b, \quad (7.24b)$$

where the prime indicates dimensional quantities and h_b is the bottom topography profile. The pressure fields are related to the thickness fields by means of the hydrostatic relation

$$p'_1 = \rho_1 g(h'_1 + h'_2 + h'_b), \quad (7.25a)$$

$$p'_2 = \rho_1 g h'_1 + \rho_2 g(h'_2 + h'_b), \quad (7.25b)$$

where the constants ρ_1 and ρ_2 denote the density of each layer.

The governing equations are nondimensionalised using scales L , U , L/U , D and $\rho_0 U^2$ for length, velocity, time, depth and pressure, respectively, and are given by

$$\frac{\partial u_\ell}{\partial t} + u_\ell \frac{\partial u_\ell}{\partial x} + v_\ell \frac{\partial u_\ell}{\partial y} = -\frac{\partial p_\ell}{\partial x} + (Ro^{-1} + \beta y)v_\ell - \sigma \mu(u_\ell - u_\ell^*) + Ro^{-1}E_H \Delta u_\ell - \sigma r \delta_{\ell,2} u_\ell,$$

$$\frac{\partial v_\ell}{\partial t} + u_\ell \frac{\partial v_\ell}{\partial x} + v_\ell \frac{\partial v_\ell}{\partial y} = -\frac{\partial p_\ell}{\partial y} - (Ro^{-1} + \beta y)u_\ell - \sigma \mu(v_\ell - v_\ell^*) + Ro^{-1}E_H \Delta v_\ell - \sigma r \delta_{\ell,2} v_\ell,$$

$$\frac{\partial h_\ell}{\partial t} + u_\ell \frac{\partial h_\ell}{\partial x} + v_\ell \frac{\partial h_\ell}{\partial y} = -h_\ell \left(\frac{\partial u_\ell}{\partial x} + \frac{\partial v_\ell}{\partial y} \right),$$

where u_ℓ and v_ℓ are eastward and northward components of the two-dimensional velocity field, respectively, for $\ell = 1, 2$. In addition, the nondimensional pressure

Table 7.1. Standard values of the fixed parameters as used in the two-layer shallow water model of Sterk et al. (2010)

Parameter	Meaning	Value	Unit
A_H	momentum diffusion coefficient	1.0×10^2	$\text{m}^2 \text{s}^{-1}$
μ	relaxation coefficient	1.0×10^{-6}	s^{-1}
r	linear friction coefficient	1.0×10^{-6}	s^{-1}
f_0	Coriolis parameter	1.0×10^{-4}	s^{-1}
β_0	planetary vorticity gradient	1.6×10^{-11}	$\text{m}^{-1} \text{s}^{-1}$
ρ_0	reference density	1.0	kg m^{-3}
ρ_1	density (top layer)	1.01	kg m^{-3}
ρ_2	density (bottom layer)	1.05	kg m^{-3}
g	gravitational acceleration	9.8	m s^{-2}
α_1	zonal velocity forcing strength (top layer)	1.0	
α_2	zonal velocity forcing strength (bottom layer)	0.5	
L_x	channel length	2.9×10^7	m
L_y	channel width	2.5×10^6	m
H_1	mean thickness (top layer)	5.0×10^3	m
H_2	mean thickness (bottom layer)	5.0×10^3	m
L	characteristic length scale	1.0×10^6	m
U	characteristic velocity scale	1.0×10^1	m s^{-1}
D	characteristic depth scale	1.0×10^3	m

terms are given by

$$p_1 = \frac{\rho_1}{\rho_0} F(h_1 + h_2 + h_b),$$

$$p_2 = \frac{\rho_1}{\rho_0} Fh_1 + \frac{\rho_2}{\rho_0} F(h_2 + h_b).$$

Several nondimensional numbers appear in the governing equations: the β parameter, the Rossby number Ro , the horizontal Ekman number E_H and the inverse Froude number F . These parameters have the following expressions in terms of the dimensional parameters:

$$\beta = \frac{\beta_0 L^2}{U}, \quad Ro = \frac{U}{f_0 L}, \quad E_H = \frac{A_H}{f_0 L^2}, \quad F = \frac{g D}{U^2}.$$

Furthermore, σ is the advective time scale L/U . Standard values of the dimensional parameters as used in Sterk et al. (2010) are listed in Table 7.1.

The dynamical equations are considered on the zonal β -plane channel

$$0 \leq x \leq L_x/L, \quad 0 \leq y \leq L_y/L.$$

All fields are supposed to be periodic in the x direction, and at $y = 0, L_y/L$, the conditions

$$\frac{\partial u_\ell}{\partial y} = \frac{\partial h_\ell}{\partial y} = v_\ell = 0$$

are imposed. The model is forced by relaxation to a westerly wind given by the profile

$$\begin{aligned} u_1^*(x, y) &= \alpha_1 U_0 U^{-1} (1 - \cos(2\pi y L / L_y)), & v_1^*(x, y) &= 0, \\ u_2^*(x, y) &= \alpha_2 U_0 U^{-1} (1 - \cos(2\pi y L / L_y)), & v_2^*(x, y) &= 0, \end{aligned}$$

where the dimensional parameter U_0 controls the strength of the forcing, and the nondimensional parameters α_1 and α_2 control the vertical shear of the forcing. For the bottom topography, a profile with zonal wave number 3,

$$h_b(x, y) = h_0 D^{-1} (1 + \cos(6\pi x L / L_x)),$$

is chosen, where the dimensional parameter h_0 controls the amplitude of the topography. The bottom topography is contained entirely in the bottom layer, which implies the restriction $h_0 \leq H_2/2$.

Observational evidence (Benzi et al., 1986) suggests that the fundamental physical processes involved in low-frequency behaviour manifest themselves at zonal wave numbers less than 5. Therefore, wave numbers $m = 0, 3$ in the zonal direction and the wave numbers $n = 0, 1, 2$ in the meridional direction were chosen. Let

$$R = \{(0, 0), (0, 1), (0, 2), (3, 0), (3, 1), (3, 2)\}$$

denote the set of retained wave number pairs. In Sterk et al. (2010), basis functions (for an integer $k \geq 0$ and a real number $\alpha > 0$)

$$c_k(\xi; \alpha) = \begin{cases} \frac{1}{\sqrt{\alpha}} & k = 0 \\ \sqrt{\frac{2}{\alpha}} \cos\left(\frac{k\pi\xi}{\alpha}\right) & k > 0, \end{cases} \quad (7.26)$$

$$s_k(\xi; \alpha) = \sqrt{\frac{2}{\alpha}} \sin\left(\frac{k\pi\xi}{\alpha}\right),$$

are used, where $\xi \in [0, \alpha]$, and the numerical factors serve as normalisation constants.

All nondimensional fields are next expanded as

$$u_\ell(x, y, t) = \sum_{(m,n) \in R} [\widehat{u}_{\ell,m,n}^c(t)c_{2m}(x; a) + \widehat{u}_{\ell,m,n}^s(t)s_{2m}(x; a)] c_n(y; b),$$

$$v_\ell(x, y, t) = \sum_{(m,n) \in R} [\widehat{v}_{\ell,m,n}^c(t)c_{2m}(x; a) + \widehat{v}_{\ell,m,n}^s(t)s_{2m}(x; a)] s_n(y; b),$$

$$h_\ell(x, y, t) = \sum_{(m,n) \in R} [\widehat{h}_{\ell,m,n}^c(t)c_{2m}(x; a) + \widehat{h}_{\ell,m,n}^s(t)s_{2m}(x; a)] c_n(y; b),$$

where $a = L_x/L$ and $b = L_y/L$. In this way the truncated expansions satisfy the boundary conditions, and a 46-dimensional system of ordinary differential equations results. As control parameters, the maximal zonal velocity of the jet U_0 and the maximum height of the topography h_0 are chosen.

For $U_0 \leq 12.2 \text{ ms}^{-1}$ there is a stable equilibrium corresponding to a steady westerly wind. This steady flow becomes unstable through Hopf bifurcations as the forcing U_0 increases. This gives rise to two types of stable waves: for lower orography (about 800 m), the period is about 10 days and there is eastward propagation in the bottom layer; for more pronounced orography, the period is longer (30–60 days), and the waves are nonpropagating. The waves can be identified as mixed baroclinic/barotropic instabilities, where the baroclinicity is not that associated to midlatitude synoptic systems (indeed, wave number 3 is not the most unstable baroclinic mode). Rather, instabilities here bear resemblance to the orographic baroclinic instability (Cessi and Speranza, 1985).

The waves remain stable in relatively large parameter domains and bifurcate into strange attractors through a number of scenarios in the parameter quadrant $U_0 \leq 14.5 \text{ m/s}$ and $h_0 \geq 850 \text{ m}$. The Lyapunov diagram (top panel of Fig 7.18) shows a classification of the dynamical behaviour in the different regions of the (U_0, h_0) plane. Bifurcations of equilibria and periodic orbits (bottom panel) explain the main features of the Lyapunov diagram. The two Hopf curves $H_{1,2}$ give birth to stable periodic orbits. In turn, these periodic orbits bifurcate into strange attractors through three main routes to chaos:

1. Period doubling cascade of periodic orbits (the curves P_1 , P_2 and P_3 in Fig. 7.18b);
2. Hopf-Neimark-Sacker bifurcation of periodic orbits (the curve T_2 in Fig. 7.18b), followed by the breakdown of a torus (cf. Section 2.4);
3. Saddle-node bifurcation of periodic orbits taking place on a strange attractor (the curve SP_4 in Fig. 7.18b), the so-called intermittency route.

The low-frequency atmospheric behaviour in this model is characterised in terms of intermittency due to bifurcations of waves. Nonpropagating planetary waves arise from the interaction of zonal flow with orography. Low-frequency behaviour with the appropriate time scales (10–200 days, where the lower-frequency components of

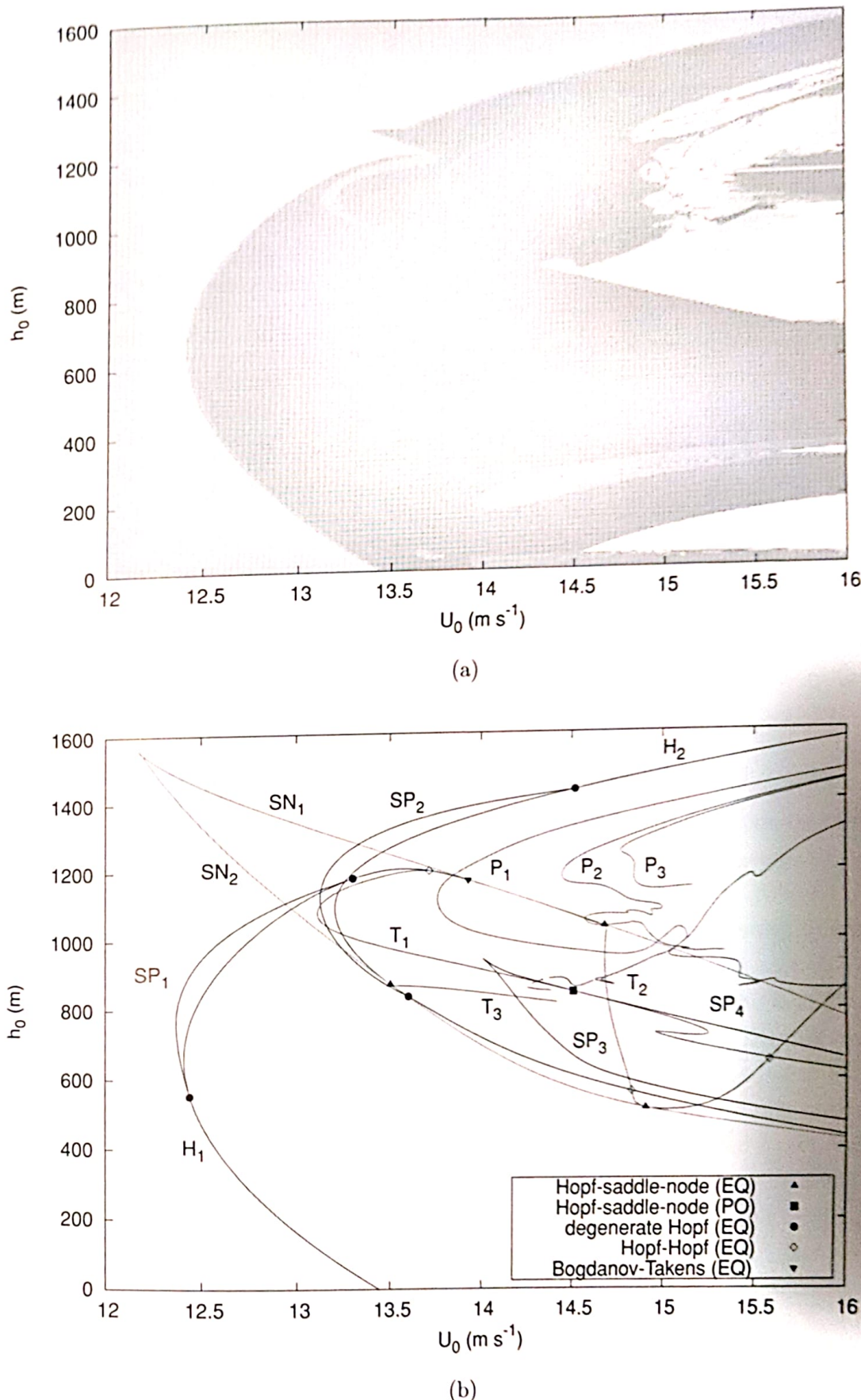


Figure 7.18 (a) Lyapunov diagram for the attractors of the system. (b) Regime diagram of attractors of the low-order model in the (U_0, h_0) parameter plane. The marked locations are codimension-2 bifurcations. The colour coding of both diagrams is provided in Table 7.2. (See Colour Plate.)

Table 7.2. Colour coding for the Lyapunov diagram and bifurcation diagram in Fig. 7.18

Colour	Lyapunov exponents	Attractor type
green	$0 > \lambda_1 \geq \lambda_2 \geq \lambda_3$	equilibrium
blue	$\lambda_1 = 0 > \lambda_2 \geq \lambda_3$	periodic orbit
magenta	$\lambda_1 = \lambda_2 = 0 > \lambda_3$	2-torus
cyan	$\lambda_1 > 0 \geq \lambda_2 \geq \lambda_3$	strange attractor
white		escaping orbit
Colour	Bifurcation type	Bifurcating attractor
green	saddle-node bifurcation	equilibrium
red	Hopf bifurcation	equilibrium
magenta	Hopf-Neimark-Sacker bifurcation	periodic orbit
grey	period doubling bifurcation	periodic orbit
blue	saddle-node bifurcation	periodic orbit

60–200 days can be interpreted as harmonics of the higher-frequency components of 10–60 days) is exhibited for physically relevant values of the parameters (realistic wind speed U_0 and topography height h_0).

7.5 Regime transitions and metastable states

In Berner and Branstator (2007), an analysis is performed of data from seven million days of output of the 500-hPa geopotential height field from an atmospheric GCM (the CCM0). Although they find statistically significant non-Gaussianities in the probability density function (in a reduced space spanned by four EOFs), they find no evidence for multiple local density maxima. They do find local maxima when conditional probability density functions are constructed by making two-dimensional slices through the four-dimensional probability space, but such features are not present in the full space. It is suggested that the non-Gaussianity of the probability density function can be attributed to a mix of a small number of Gaussian components, of which two are dominant (corresponding to a Pacific blocked state and zonal state).

These results can be understood by so-called Hidden Markov Models (HMMs) (Majda, 2006; Franzke et al., 2008). An HMM is designed to provide a description of a stochastic dynamical system for which one has only partial information. Let Y_t be the observed random variable and assume that the statistics of Y_t are dependent on a hidden (non-observable) discrete variable $X_t = X_{t_k}, k = 1, \dots, N$, which is governed by a so-called Markov chain, that is,

$$P(X_{n+1} = x | X_1 = x_1, \dots, X_n = x_n) = P(X_{n+1} = x | X_n = x_n). \quad (7.27)$$

The transitions between the different states in the Markov chain are described by a transition probability matrix A .

An HMM hence consists of a set S of N hidden states $S = \{s_1, \dots, s_N\}$, and the hidden variable X takes values on this set, $X_t \in S$. The coefficients of the transition probability matrix A are given by $a_{ij} = P(X_t = s_j | X_{t-1} = s_i)$. The dependence of the probability distributions of Y_t on X_t is described using the conditional probabilities $B_i = P(Y_t | X_t = s_i)$. Given the initial distribution $P(X_1)$, the joint probability distribution is then given by

$$P(X_1, \dots, X_T, Y_1, \dots, Y_T) = P(X_1)P(Y_1 | X_1) \prod_{t=2}^T P(X_t | X_{t-1})P(Y_t | X_t). \quad (7.28)$$

When only a time series of Y_t is available, parameters in the HMM must be estimated (given a prescribed number of hidden states N), and algorithms to do so are provided in Franzke et al. (2008).

As an example, consider the two-state ($N = 2$) Markov chain with the transition probability matrix (Franzke et al., 2008)

$$A = \begin{bmatrix} 0.99 & 0.01 \\ 0.01 & 0.99 \end{bmatrix}, \quad (7.29)$$

and two univariate distributions $B_1 = N(3.0, 1.0)$ and $B_2 = N(-3.0, 2.0)$, where $N(\mu, \sigma^2)$ is the normal distribution with mean μ and variance σ^2 . If the system is in the hidden state X_1 , the observed signal Y_t is drawn randomly from B_1 ; otherwise it is drawn from B_2 . When in state X_1 , the probability to stay in state X_1 or switch to state X_2 is given by a_{11} and a_{12} , respectively.

A typical realisation of Y_t versus time is presented in Fig. 7.19, where the existence of two distinct regime states can be seen (left panel of Fig. 7.19) and the resulting probability density function is bimodal (right panel of Fig. 7.19). The middle panel of Fig. 7.19 shows the most probable hidden state sequence, the so-called Viterbi path. With overlapping Gaussian distributions $B_1 = N(1.0, 1.7)$ and $B_2 = N(-0.5, 1.2)$, the probability distribution is neither bimodal nor Gaussian.

If the state space S of X can be decomposed into two or more sets with relatively infrequent transitions between these sets, the Markov chain is said to be **metastable**. The presence of metastability allows for a time scale separation between ‘fast’ transitions within metastable sets and the ‘slow’ transitions between metastable sets. The eigenvalues λ of the transition probability matrix A provide information on metastability, as is illustrated using the example that follows.

Consider the Itô SDE given by (Franzke et al., 2008)

$$Y_t = (-4Y_t^3 - c(3Y_t^2 - 1))dt + \sigma dW_t, \quad (7.30)$$

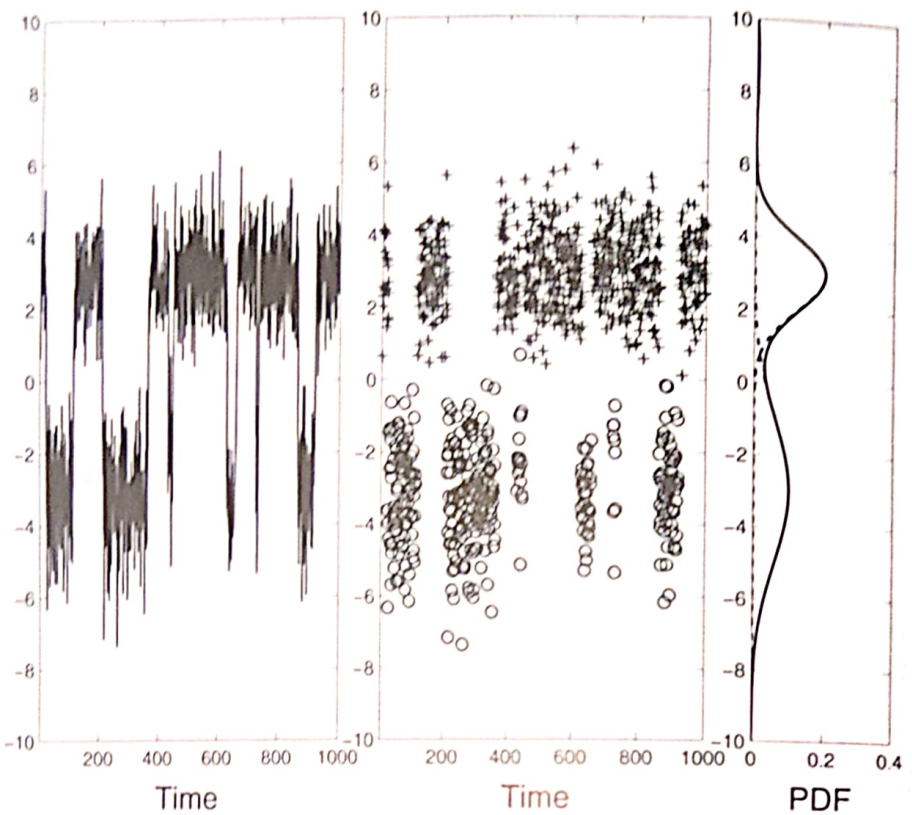


Figure 7.19 Realisation of the two-state HMM with transition probability matrix (7.29) and Gaussian distributions B_1 and B_2 (figure from Franzke et al., 2008).

where the first term is the gradient of the potential $V(y) = y^4 + cy(y-1)(y+1)$, which is shown for $c = 0.22$ in Fig. 7.20a. It is shown in Franzke et al. (2008) that if

$$c_k = \frac{1}{\Delta t} \log \lambda_k, \quad (7.31)$$

where Δt is the time step used to construct A , then metastability is characterised by $0 = c_1 > Re(c_2) \geq Re(c_3) \dots \geq Re(c_N)$. Such conditions are shown to apply for (7.30) when $c = 2.2$ (Fig 7.20).

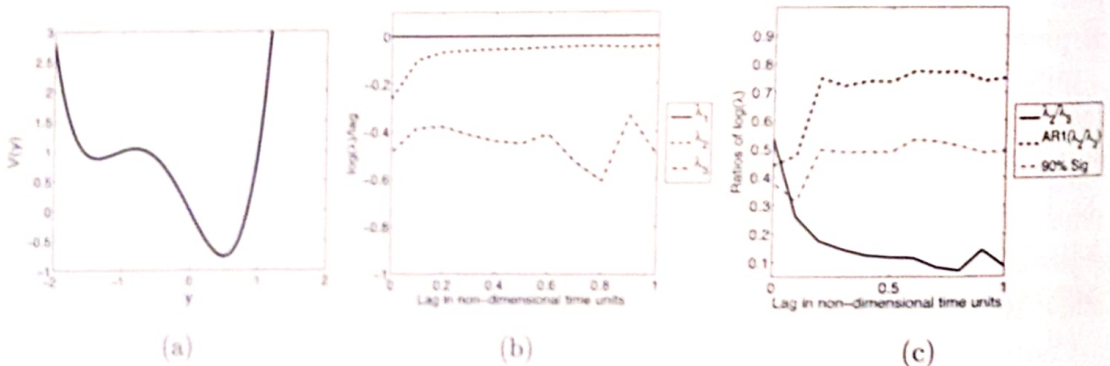


Figure 7.20 (a) Potential $V(y)$ of the system (7.30) for $c = 2.2$. (b) Modified eigenvalues c_k , for $N = 3$, and (c) ratio of eigenvalues (figure from Franzke et al., 2008).

In Franzke et al. (2008), an HMM analysis is also provided of output of a quasi-geostrophic barotropic model of flow over topography. The dimensionless equations for this model (on a $2\pi \times 2\pi$ periodic domain) are given by

$$\frac{\partial q}{\partial t} + \mathbf{u} \cdot \nabla q + U \frac{\partial q}{\partial x} + \beta \frac{\partial \psi}{\partial x} = 0, \quad (7.32a)$$

$$q = \nabla^2 \psi + h, \quad (7.32b)$$

$$\frac{dU}{dt} = \frac{1}{4\pi^2} \int_V h \frac{\partial \psi}{\partial x} d^2x, \quad (7.32c)$$

where q is the potential vorticity, ψ the streamfunction, \mathbf{u} the geostrophic velocity vector, U the mean zonal flow velocity and h the topography. The latter is taken as $h = h_0(\cos x + \sin x)$, and the HMM is constructed from model output of simulations with different values of h_0 . For $h_0 = 1.06$ and $\beta = 1$, the HMM analysis with $N = 3$ indicates metastability based on the eigenvalues of the transition probability matrix A .

The first hidden state represents a blocking-like flow, and the other two states represent a zonal circulation with different magnitudes. As can be seen, the probability density function of U is nearly Gaussian distributed, and the three conditional probability density distributions of the hidden Markov states have a substantial overlap (see Fig. 7.21). The skewness in the distribution of U is mainly due to the presence of state 1 (the blocking state).

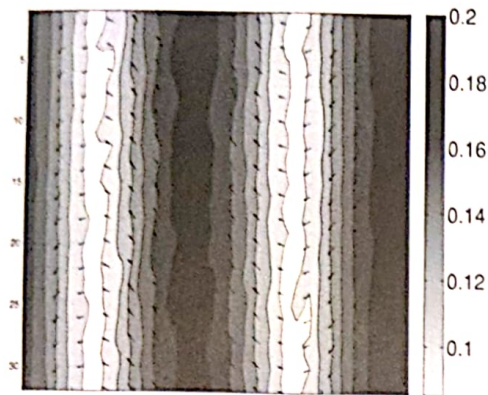
7.6 Synthesis

In this chapter, we dealt with a classical problem in the theory of the general atmospheric circulation, that is, the characterisation of recurrent flow patterns observed at midlatitudes in the Northern Hemisphere winters. The problem is important in understanding the persistence and predictability of atmospheric motion beyond the time scales of baroclinic synoptic disturbances (2–5 days). Indeed, it is expected that insight into the nature of low-frequency regime dynamics will lead to significant progress in the so-called extended range weather forecasting.

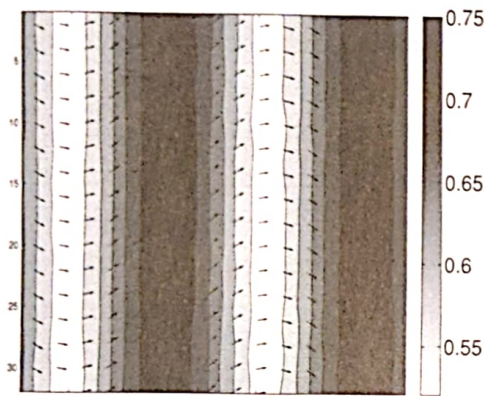
At the same time, the problem is of great relevance in climate science, because it has been suggested that climate change predominantly manifests itself through changes in the atmospheric circulation regimes, that is, ‘changes in the probability density function of the climate attractor’ (Corti et al., 1999). In fact, misrepresentation of the statistics of blocking and planetary waves is widespread in climate models (Lucarini et al., 2007; Palmer et al., 2008): this may have a profound impact on the ability of such models to reproduce both current climate and climate change.

There are different approaches to the problem of low-frequency atmospheric variability. In this chapter, we presented an overview of the dynamical systems approach, where attractors and the behaviour of trajectories is studied within a hierarchy of

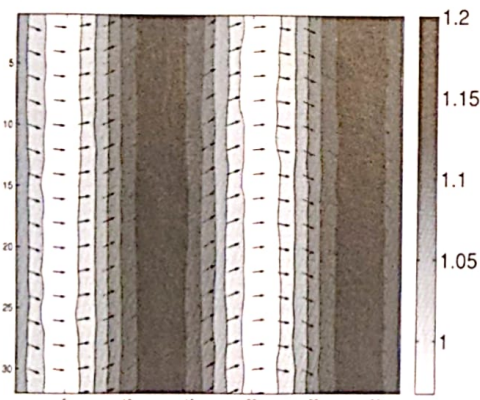
a) Hidden State 1



b) Hidden State 2



c) Hidden State 3



(d)

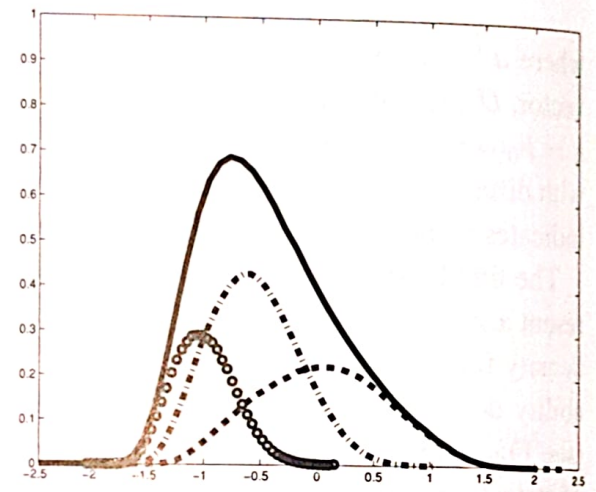


Figure 7.21 Velocity field corresponding to the hidden states of the HMM of the model (7.32), with (a) blocked state 1, (b) zonal flow state 2, and (c) zonal flow state 3. (d) Probability density distribution of U and (weighted) conditional probability density distributions of the hidden states (state 1: dashed; state 2: dashed-dotted and state 3: circles) for a topographic height $h_0 = 1.06$ (figure from Franzke et al., 2008).

models. From the material presented, the atmospheric flow is susceptible to many different type of instabilities (barotropic, baroclinic, topographic/orographic). These instabilities give rise to multiple steady states, multiple limit cycles, tori and more complex attractors, the latter having positive Lyapunov exponents (cf. Fig. 7.18).

A trajectory is expected to display a complicated path through phase space, as is indeed the case in even relatively simple atmospheric models. As we saw in Section 7.1, atmospheric low-frequency variability is characterised by only a few dominant regimes and specific intraseasonal oscillations, with only a few patterns involved. How do these patterns arise from so complex trajectories in phase space?

Orographic resonance theories lend support to the hypothesis that activity of planetary waves possesses a multimodal distribution (Benzi et al., 1986). Highly truncated barotropic models provide a relatively simple view on the origin of the multimodality. From the three-mode model of Charney and DeVore (1979) discussed in Section 7.3.2, it follows that the interaction between zonal flow and wave field causes the occurrence of two equilibria for the amplitude of planetary waves. Legras and Ghil (1983) found intermittent transitions between multiple equilibria representing blocked and zonal flows. Crommelin et al. (2004) explain the transitions in terms of homo- and heteroclinic dynamics near equilibria corresponding to distinct preferred flow patterns (Section 7.3.3). Sterk et al. (2010) add the element of intermittency due to bifurcations of waves to the mechanisms of low-frequency variability (Section 7.4.3).

In the higher-dimensional dynamical systems (quasi-geostrophic and shallow-water) models, a multitude of (mostly unstable) steady states (real fixed points) exists. Trajectories appear to be affected by these unstable fixed points, so clearly seen in the results of Itoh and Kimoto (1996). This is explained in Crommelin et al. (2004) and Sterk et al. (2010) because the multiple steady states are responsible for heteroclinic connections, leading to complicated temporal behavior with only a few patterns involved.

The transitions between different regions in phase space of slow dynamics (or regimes) can be induced by chaotic itinerary (Itoh and Kimoto, 1996) or can occur along unstable periodic orbits (Selten and Branstator, 2004). A more kinematic view of the transitions is provided by a Markov chain model where a matrix of probabilities for transition from one regime to another is determined based on the expected residence time of the trajectory in each regime. Using this approach, Mo and Ghil (1988), for example, found that transitions between regimes in observations tend to avoid, rather than favour, passages through the climatological mean. Many trajectories in the results previously discussed display specific low-frequency (40–70 days) oscillatory behaviour associated with (stable or unstable) periodic orbits, which can coexist with the regime switches (Itoh and Kimoto, 1996). These prototypes of intraseasonal oscillations essentially depend on the existence of the orography (Keppenne et al., 2000). Patterns of these oscillations also show a close correspondence with those in observations (Kondrashov et al., 2004).

Hence, from the dynamical systems viewpoint, the atmospheric low-frequency variability characterising the Northern Hemisphere midlatitude circulation results from dynamical processes specific to the interaction of zonal flow and planetary waves with orography. The phase space is occupied with clusters of slow dynamics

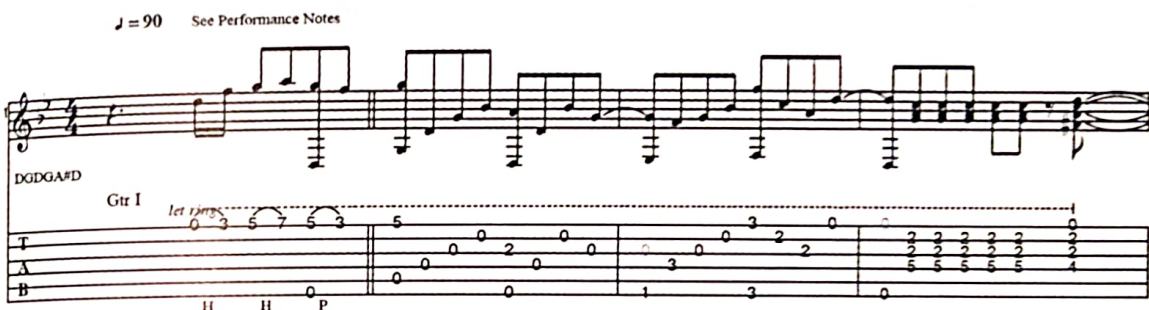
(the regimes) where a trajectory displays low-frequency variability within each cluster with a related pattern. Transitions between the different clusters can occur through noise or deterministic dynamics; hidden Markov chain models as presented in Section 7.5 are a nice tool to model these transitions (Majda et al., 2006, Franzke et al., 2008).

Despite this remarkable research effort, the scientific debate is still very much open on whether a single equilibrium (Ambaum, 2008; Nitsche et al., 1994; Stephenson et al., 2004; Berner and Branstator, 2007) or multiple equilibria (Hansen and Sutera, 1995; Mo and Ghil, 1988; Ruti et al., 2006) characterise the large-scale midlatitude atmospheric circulation. Quite a gap still exists to interpret observations and results of high-resolution atmospheric models with the results of two-layer quasi-geostrophic and shallow-water models. The idealised dynamical models do not capture the time-mean state, all relevant patterns and, consequently, the transitions among them, very well. A nice bridge may be the laboratory work on barotropic flow over topography (Weeks et al., 1997; Tian et al., 2001) where clearly regime-type behaviour is found in a realistic flow (instead of a truncated model).

However, observational time series are still too short to extract transition probabilities between regimes with statistical significance. It is not clear whether nonlinear interactions of waves of different spatial scales play an essential role in the onset or the maintenance of low-frequency atmospheric variability. Alternative mechanisms have also been proposed; the low-frequency large-scale pattern of the North Atlantic Oscillation is found, in Benedict et al. (2004), to result from breaking of synoptic scale waves, where the anticyclonic (cyclonic) wave breaking evolves into the positive (negative) NAO phase. A description of this and other alternative mechanisms (Athansiadis and Ambaum, 2010; Jin, 2010) is clearly outside the scope of this chapter.

8

El Niño Variability



A swinging theory
DGDGA[♯]D, California Dreamin', Chris Proctor

About once every four years, the sea-surface temperature in the Eastern Equatorial Pacific is a few degrees higher than normal (Philander, 1990). Near the South American coast, this warming of the ocean water is usually at its maximum around Christmas. Long ago, Peruvian fishermen called it El Niño, the Spanish phrase for the Christ Child.

8.1 Phenomena

During the past several decades, El Niño has been observed in unprecedented detail thanks to the implementation of the TAO/TRITON array and the launch of satellite-borne instruments (McPhaden et al., 1998). The relevant quantities to characterise the state in the equatorial ocean and atmosphere are sea level pressure, sea-surface temperature (SST), sea level height, surface wind and ocean subsurface temperature.

The annual mean state of the equatorial Pacific sea-surface temperature is characterised by the zonal contrast between the western Pacific “warm pool” and the “cold tongue” in the eastern Pacific. The mean temperature in the eastern Pacific is approximately 23°C, with seasonal excursions of about 3°C. What makes El Niño unique